Computers and Geotechnics 196 (2026) 108114

Contents lists available at ScienceDirect

Computers and Geotechnics

journal homepage: www.elsevier.com/locate/compgeo

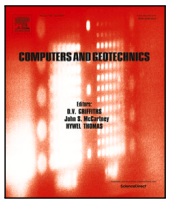

Research paper

# A cohesive zone model for fatigue under cyclic thermo-hydro-mechanical loading

Wen Luo [a,b,*], Anne-Catherine Dieudonné [a], Josselin Ouf [a,b], Florian Amann [b], Philip J. Vardon [a]

[a] Faculty of Civil Engineering and Geosciences, Delft University of Technology, Delft, 2628 CN, The Netherlands
[b] Department of Engineering Geology and Hydrogeology, RWTH Aachen, Aachen, D-52064, Germany

ARTICLE INFO

*Keywords:*
Fracturing
Thermo-hydro-mechanics
Geothermal energy
Cohesive zone model

ABSTRACT

Rocks can undergo fatigue failure when subjected to cyclic mechanical, hydraulic, or thermal loadings, or a combination of these. Therefore, accounting for possible fatigue damage is important for subsurface engineering projects, such as the cyclic stimulation of geothermal reservoirs. However, existing models do not simultaneously account for degradation of both tensile strength and stiffness under varying-amplitude loading and coupled thermo-hydro-mechanical (THM) conditions. To address this, a new cohesive zone model is developed to account for the effect of fatigue on tensile strength and stiffness. The model is then used within the framework of zero-thickness interface elements to simulate the response of pre-existing or new fractures. Hydraulic and thermal processes are included in both the cohesive interface elements and the continuum elements, allowing the consideration of coupled thermo-hydro-mechanical processes. The fatigue damage variable is set to evolve with the number and magnitude of cycles according to Palmgren-Miner's rule. The proposed method is validated against three laboratory tests from the literature, including cyclic Brazilian test, cyclic hydraulic fracturing test and cyclic thermal stimulation test. All three validation results show that the fatigue damage or reduced breakdown pressure can be well reproduced. Mesh sensitivity based on the simulation of the Brazilian test, in which interface elements are inserted in-between all the continuum elements, highlights the influence of the mesh orientation and mesh density on the simulation results. In addition, stabilisation of the method is demonstrated by increasing the mechanical viscosity, which must be used with care to avoid predicting a longer fatigue life. The ability of the method to handle varying-amplitude cyclic loading is demonstrated by the simulation of a synthetic cyclic loading scheme based on the Brazilian test. The proposed method can be used to support the design of cyclic thermal stimulation campaigns for geothermal (or other) reservoirs, by being able to simulate the reduction in strength due to fatigue, and thus reducing stimulation pressures needed.

## 1. Introduction

Rock fatigue failure is a common phenomenon in subsurface engineering projects, and can be either beneficial (e.g., fatigue cracks near geothermal or hydrocarbon wells (Hofmann et al., 2021; Zang et al., 2025)) or detrimental (e.g., fatigue damage of dams (Meng et al., 2023)). The fatigue damage of rocks subjected to cyclic mechanical, hydraulic or thermal loading has been extensively studied, demonstrating that rock strength can be reduced and that fracture patterns can become more complex under cyclic loading (Cerfontaine and Collin, 2018; Zang et al., 2021; Jung et al., 2021; Niu et al., 2023). For example, cyclic Brazilian tests conducted by Erarslan and Williams (2012) and Liu et al. (2018) have shown that rock samples fail under lower ultimate loads and exhibit different fracturing mechanism compared to those under monotonic loading.

In addition to pure mechanical loading, coupled hydro-mechanical and thermo-mechanical loadings have also been used to induce fatigue damage in rocks. Laboratory cyclic hydraulic fracturing tests on sandstone and granite samples have shown significant reductions in breakdown pressure (up to 20% for Pocheon granite cores (Zhuang et al., 2019), 7.18%–18.9% for Xujiahe sandstone (Kang et al., 2020), and 16% for dry Tennessee sandstone) (Patel et al., 2017). Laboratory tests have also shown that cyclic hydraulic stimulation can lead to the formation of more complex fracture networks, as opposed to the simpler fractures typically induced by conventional hydraulic stimulation (Patel et al., 2017; Wei et al., 2023). Moreover, the effectiveness of

* Corresponding author at: Faculty of Civil Engineering and Geosciences, Delft University of Technology, Delft, 2628 CN, The Netherlands.
*E-mail address:* W.Luo@tudelft.nl (W. Luo).

https://doi.org/10.1016/j.compgeo.2026.108114
Received 25 July 2025; Received in revised form 28 February 2026; Accepted 30 March 2026
Available online 21 April 2026

cyclic hydraulic fracturing has been demonstrated in field-scale tests, such as the cyclic hydraulic stimulation of well PX-1 at the Pohang enhanced geothermal system (EGS) project site, South Korea, which demonstrated that cyclic injection was able to improve well performance while ensuring that seismic activity remains below the target threshold of $M_w$ 2.0 (Hofmann et al., 2019; Zang et al., 2021). In addition, cyclic heating–cooling treatment on rocks can also reduce their strength, which has been demonstrated in experiments (Gasc-Barbier et al., 2014; Zhu et al., 2020). However, study of rock fatigue damage under cyclic fully coupled thermo-hydro-mechanical (THM) loadings is rarely reported. Cyclic THM processes can happen during, for example, soft stimulation of geothermal reservoirs. A combination of thermal stress and fatigue damage may further accelerate the rock failures. Therefore, the investigation of the rock fatigue damage under cyclic THM loadings is necessary and meaningful, while existing literature mainly focuses on individual loadings and simple hydro-mechanical or thermo-mechanical loadings.

Numerical simulation provides an essential tool for understanding fatigue damage of rocks. Incorporating fatigue damage into the cohesive zone model is a common method to predict the onset and propagation of fatigue fractures. The cohesive zone model was first proposed by Dugdale (1960) and Barenblatt (1962) to circumvent the unrealistic infinite stresses at the fracture tip obtained for a linear elastic material, assuming a cohesive-law governed zone in front of the fracture tip. Later, Hillerborg et al. (1976) introduced CZM into FEM to simulate crack initiation and growth in concrete. When discretising the material domain, the material separation and thus damage of the structure can be described by interface elements in-between continuum elements (Scheider, 2001), governed by the cohesive law that relates traction and separation of the two surfaces of the interface element. It has the advantages of being capable of simulating fracture initiation, an intuitive physical meaning and its mitigation of the need to calculate the stress singularity at the fracture tip over other approaches like extended finite element method. The traction–separation law, consisting of elastic and softening curves, is controlled by two material parameters, i.e. the critical fracture energy $G_I$ (for mode-I fracture) and the tensile strength $\sigma_{n0}$, shown in Fig. 2(a). The damage of the rock, after the tensile strength is reached, is described by the softening curve.

Traditionally, the law can only describe damage due to monotonic loading beyond a strength threshold, i.e. if loading remains below the strength, the behaviour is elastic, with no additional damage, regardless of the number of loading cycles. Previous efforts have been made to incorporate fatigue damage due to cyclic loading into cohesive laws (Roe and Siegmund, 2003; Maiti and Geubelle, 2005; Robinson et al., 2005; Turon et al., 2007; Khoramishad et al., 2010; De Moura and Gonçalves, 2015; Choi et al., 2020; Xi et al., 2021; Wei et al., 2023). For example, Robinson et al. (2005) incorporated a fatigue damage variable into the cohesive law based on a modified Paris power law equation, which relates the fatigue crack growth rate ($\mathrm{d}a/\mathrm{d}N$, $a$ is the fatigue crack length and $N$ the number of cycles) to the amplitude of the applied stress intensity factor ($\Delta K = K_{max} - K_{min}$, $K_{max}$ is the maximum stress intensity factor while $K_{min}$ the minimum). The model was used to simulate delamination growth in composite material and their numerical results showed that the model can reproduce the characteristics of the Paris power law that is commonly observed in experiments, though the model considers only the maximum load. Munoz et al. (2006) further extended the work of Robinson et al. (2005) to consider the cyclic loads with non-zero minimum value. Turon et al. (2007) developed a cohesive zone model with a single damage variable and related the damage state with the number of cycles and the loading conditions. Khoramishad et al. (2010) integrated a strain-based fatigue damage with the cohesive law to simulate the impact of cyclic loading on the bonded joints. Unlike most of the previous models, the degradation of the cohesive strength is possible and dependent on the fatigue damage, making it possible to accumulate fatigue damage before the cohesive separation stage is reached. Xi et al. (2021) and Wei et al. (2023) followed this concept but formulated the fatigue damage variable as a function of the number of cycles. One limitation in those models is that the cohesive stiffness remains unchanged in the elastic stage. In contrast, some other literatures, e.g. Nojavan et al. (2016a) and Choi et al. (2020), presented the computation of the damage evolution during cyclic loading is in conjunction with an unloading–reloading relation in the cohesive zone model, while allowing the degradation of the reloading stiffness.

While existing models have advantages and limitations in incorporating and computing fatigue damage, none address fully coupled thermo-hydro-mechanical loading, which requires the consideration of the thermal processes in the cohesive interface element. In addition, a specific cracking path was prescribed along a pre-defined line in most of the modelling exercises in the previously mentioned literature, while the cases where fracture can initiate and propagate in the most efficient fracturing paths are not considered. These limitations render the models unsuitable for simulating fatigue failure in, e.g. geothermal reservoirs, where fractures can propagate in arbitrary but most efficient direction. In addition, the re-loading stiffness is unchanged if the traction–separation path is in the elastic stage in previous models (Khoramishad et al., 2010; Xi et al., 2021; Wei et al., 2023), which fails to capture the observed degradation of rock stiffness and the accumulation of deformation (Cerfontaine and Collin, 2018; Xiao et al., 2010). Wei et al. (2023) also formulated the fatigue damage variable as a function of the number of cycles under constant-amplitude loading, which does not consider varying-amplitude cyclic loading.

In this paper, we introduce a fatigue damage variable into the cohesive zone model, which, together with cohesive interface elements and continuum elements that consider fully coupled THM processes, can simulate fatigue failures under cyclic THM loading. While the principles of the formulation can apply to mixed mode (shear and tension) damage, we consider tensile fatigue for clarity and due to the stress path in near well-bore conditions where thermo-hydraulic stimulation may be considered. The fatigue damage variable is calibrated using the number of loading cycles and fatigue life at different load intensities (S–N curve, or stress-number of cycles curve). With this formulation, the tensile strength and stiffness of the interface element both degrade with increasing number of cycles. Palmgren-Miner's rule is used to account for varying-amplitude cyclic loading. While the traction–separation law is temperature-invariant, the thermal expansion and contraction of the continuum elements lead to stress changes, which can generate cyclic stresses under varying temperature cycles, and therefore includes the impact of thermally-induced stresses. The proposed method is validated against three laboratory tests from the literature, including cyclic Brazilian test, cyclic hydraulic fracturing test and cyclic thermal stimulation test to demonstrate its ability to capture fatigue damage under cyclic coupled THM processes, including varying amplitude loading. The proposed model can be used to simulate cyclic thermo-hydraulic stimulation in subsurface projects, e.g. geothermal projects, and rock failures in subsurface infrastructure projects, e.g. the damaged zone under cyclic THM loading around radioactive waste repositories.

## 2. Method

### 2.1. Modelling approach

Continuum finite elements are employed to represent intact rock, whereas zero-thickness three-node interface elements are used to model discontinuities (Fig. 1). The interface elements can be inserted between continuum elements along a pre-defined path to model pre-existing fractures or weak planes, or can be placed between all continuum elements to enable arbitrary cracking paths. The interface element has a total of 9 nodes, equally distributed on top, mid, and bottom planes. The bottom and top faces of the interface element share nodes with

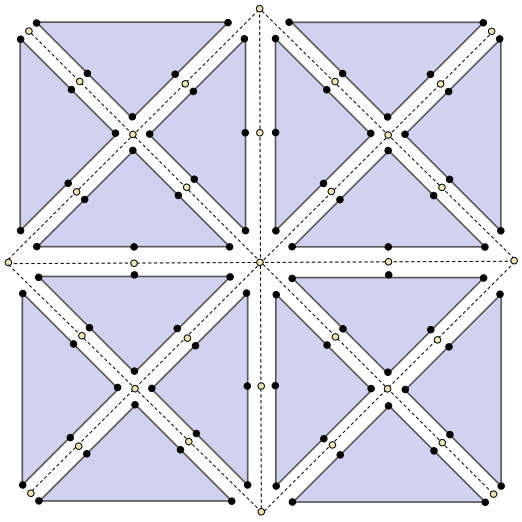

(a) Insertion of interface elements between continuum elements.

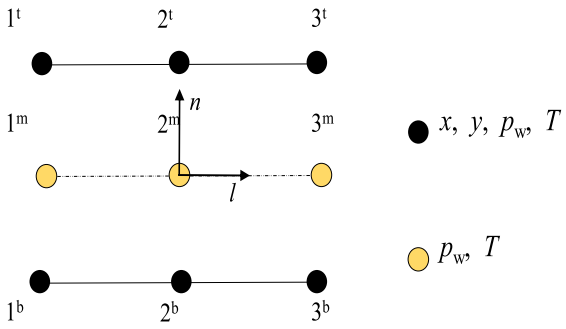


(b) Interface element.

**Fig. 1.** Finite elements used. (a) Interface elements between continuum elements to represent pre-existing or potential cracking paths. (b) Node numbering, nodal degrees of freedom and local basis for the interface element (Luo et al., 2025).

the continuum elements, each having four degrees of freedom at each node, corresponding to the $x$ and $y$ coordinates, water pressure $p_{\mathrm{w}}$, and temperature $T$. The mid-plane nodes have only two degrees of freedom for water pressure $p_{\mathrm{w}}$ and temperature $T$. In this way, different constitutive laws can be used for the continuum and the discontinuities, allowing for a more flexible representation of heat and fluid flows along and across the fracture (Luo et al., 2025). Therefore, such interface elements can be used for applications where an explicit representation of the mid-plane pressure and temperature is convenient, such as the interfaces between permeable and impermeable materials.

### 2.2. Governing equations for the continuum porous medium

The governing equations for the continuum elements follow the formulation proposed by Collin et al. (2002). The theoretical framework is composed of three balance equations, namely the water mass balance equation, the balance of momentum (or stress equilibrium) equation, and the energy balance equation. These equations, together with the necessary constitutive laws, are presented below.

#### 2.2.1. Hydraulic problem

The water mass balance equation reads:

$$\frac{\partial(\phi\rho_{\mathrm{w}})}{\partial t} + \nabla\cdot(\rho_{\mathrm{w}}\mathbf{v}_{\mathrm{w}}) = 0 \tag{1}$$

where $\phi$ is the porosity, $\rho_{\mathrm{w}}$ [kg/m$^3$] is the water density, $t$ [s] is time, and $\mathbf{v}_{\mathrm{w}}$ [m/s] the Darcy velocity vector. The water density is a function of both water pressure $p_w$ [Pa] and temperature $T$ [K] according to:

$$\rho_w = \rho_{w0}\left[1 + \frac{p_w - p_{w0}}{\kappa_w} - \beta_w\left(T - T_0\right)\right] \tag{2}$$

where $\rho_{w0}$ is the water density at the reference pressure $p_{w0}$ and reference temperature $T_0$, $\kappa$ [1/Pa] is the water compressibility, and $\beta_w$ [1/K] is the thermal expansion coefficient.

The Darcy velocity vector (neglecting gravity) is defined as:

$$\mathbf{v}_{\mathrm{w}} = -\frac{K}{\mu_{\mathrm{w}}}\nabla p_{\mathrm{w}} \tag{3}$$

where $K$ [m$^2$] is the intrinsic permeability, and $\mu_{\mathrm{w}}$ [Pa s] is the water dynamic viscosity, which is a function of temperature according to Ewen and Thomas (1989):

$$\mu_{\mathrm{w}} = 0.6612\,(T - 229)^{-1.562} \tag{4}$$

#### 2.2.2. Mechanical problem

If equilibrium state is assumed and if gravity is neglected, the balance of momentum reads:

$$\nabla\cdot\boldsymbol{\sigma} = \mathbf{0} \tag{5}$$

where $\boldsymbol{\sigma}$ [Pa] is the Cauchy's total stress tensor.

The behaviour of the intact rock is assumed to follow a linear elastic law. Assuming that compressive stress and strain are defined as negative, the thermo-poro-elastic constitutive law reads:

$$\Delta\boldsymbol{\sigma} = \mathbb{C} : \Delta\boldsymbol{\epsilon} - \Delta p_{\mathrm{w}}\boldsymbol{I} - \beta_{\mathrm{b}}K_{\mathrm{b}}\Delta T\,\boldsymbol{I} \tag{6}$$

where $\mathbb{C}$ is the 4th-order elastic stiffness tensor, $\boldsymbol{\epsilon}$ is the strain tensor, $\boldsymbol{I}$ is the 2nd-order identity tensor, $\beta_{\mathrm{b}}$ is the bulk volumetric thermal expansion coefficient, and $K_{\mathrm{b}}$ [Pa] is the drained bulk modulus.

#### 2.2.3. Thermal problem

Under the assumption of local thermal equilibrium, with no internal source or sink, the energy balance equation reads:

$$\frac{\partial\left[\left(\rho c_p\right)_{\mathrm{b}}T\right]}{\partial t} + \nabla\cdot\boldsymbol{q}_{\mathrm{T}} = 0 \tag{7}$$

where $(\rho c_p)_{\mathrm{b}}$ is the bulk volumetric heat capacity and $\boldsymbol{q}_{\mathrm{T}}$ [J/(m$^2$ s)] is the heat flux vector. The bulk volumetric heat capacity is given by:

$$\left(\rho c_{\mathrm{p}}\right)_{\mathrm{b}} = (1-\phi)\left(\rho_{\mathrm{s}}c_{\mathrm{ps}}\right) + \phi\left(\rho_{\mathrm{w}}c_{\mathrm{pw}}\right) \tag{8}$$

where $c_{\mathrm{p}}$ [J/(kg K)] is the phase specific heat capacity, $\rho$ is the phase density, and the subscripts s and w refer to the solid and water phases, respectively.

The heat flux vector is given by:

$$\boldsymbol{q}_{\mathrm{T}} = -\lambda_{\mathrm{b}}\nabla T + \rho_{\mathrm{w}}c_{\mathrm{pw}}\boldsymbol{q}_{\mathrm{D}}T \tag{9}$$

where the first term corresponds to Fourier's law and the second term corresponds to heat advection due to water flow. $\lambda_{\mathrm{b}}$ [J/(m s K)] is the bulk thermal conductivity, given by:

$$\lambda_{\mathrm{b}} = (1-\phi)\,\lambda_{\mathrm{s}} + \phi\lambda_{\mathrm{w}} \tag{10}$$

where $\lambda_{\mathrm{s}}$ and $\lambda_{\mathrm{w}}$ are the thermal conductivities of the solid and water phases, respectively.

### 2.3. Governing equations for the discontinuities

The mechanical and hydraulic governing equations for the interface elements are inherited from Luo et al. (2025) with the gas phase being neglected. Additionally, the governing equations for thermal processes are included here. Note that the following equations are tailored for 2D problems.

#### 2.3.1. Hydraulic problem

The mass balance for water in a differential volume of discontinuity $w\mathrm{d}l$ reads:

$$\frac{\partial}{\partial t}(w\rho_{\mathrm{w}}) + \frac{\partial q_{\mathrm{w}}^{\mathrm{l}}}{\partial l} - q_{\mathrm{w}}^{\mathrm{b}} - q_{\mathrm{w}}^{\mathrm{t}} = 0 \tag{11}$$

where $w$ [m] is the width of the discontinuity, $q_{\mathrm{w}}^{\mathrm{l}}$ [kg/(m s)] is the longitudinal water mass flux, and $q_{\mathrm{w}}^{\mathrm{b}}$ and $q_{\mathrm{w}}^{\mathrm{t}}$ [kg/(m$^2$ s)] are the transversal water mass fluxes incoming to the discontinuity from surrounding continuum medium.

The mass fluxes in Eq. (11) can be expanded as:

$$q_{\mathrm{w}}^{\mathrm{l}} = \rho_{\mathrm{w}} v_{\mathrm{w}}^{\mathrm{l}}; \quad q_{\mathrm{w}}^{\mathrm{b}} = \rho_{\mathrm{w}} v_{\mathrm{w}}^{\mathrm{b}}; \quad q_{\mathrm{w}}^{\mathrm{t}} = \rho_{\mathrm{w}} v_{\mathrm{w}}^{\mathrm{t}} \tag{12}$$

where $v_{\mathrm{w}}^{\mathrm{l}}$ [m$^2$/s], $v_{\mathrm{w}}^{\mathrm{b}}$ [m/s] and $v_{\mathrm{w}}^{\mathrm{t}}$ [m/s] are the longitudinal and transversal (top and bottom) volumetric fluxes. These fluxes are obtained from the following generalised Darcy's law:

$$v_{\mathrm{w}}^{\mathrm{l}} = -\frac{t^{\mathrm{l}}}{\mu_{\mathrm{w}}}\frac{\partial p_{\mathrm{w}}^{\mathrm{m}}}{\partial l}; \quad v_{\mathrm{w}}^{\mathrm{b}} = -\frac{k^{\mathrm{b}}}{\mu_{\mathrm{w}}}\breve{p}_{\mathrm{w}}^{\mathrm{b}}; \quad v_{\mathrm{w}}^{\mathrm{t}} = -\frac{k^{\mathrm{t}}}{\mu_{\mathrm{w}}}\breve{p}_{\mathrm{w}}^{\mathrm{t}} \tag{13}$$

where $t^{\mathrm{l}}$ [m$^3$] is the longitudinal hydraulic coefficient, $k^{\mathrm{b}}$ [m$^2$] and $k^{\mathrm{t}}$ [m$^2$] are the transversal permeability of the interface, $p_{\mathrm{w}}^{\mathrm{m}}$ [Pa] is the water pressure at the middle plane, defined as positive if larger than atmospheric pressure (101.325 kPa). $\breve{p}_{\mathrm{w}}^{\mathrm{b}}$ [Pa] and $\breve{p}_{\mathrm{w}}^{\mathrm{t}}$ [Pa] are the transversal pressure jumps between the bottom and top faces and the mid-plane, respectively. The transversal pressure drops are defined as follows:

$$\breve{p}_{\mathrm{w}}^{\mathrm{b}} = (p_{\mathrm{w}}^{\mathrm{m}} - p_{\mathrm{w}}^{\mathrm{b}}); \quad \breve{p}_{\mathrm{w}}^{\mathrm{t}} = (p_{\mathrm{w}}^{\mathrm{m}} - p_{\mathrm{w}}^{\mathrm{t}}) \tag{14}$$

where $p_{\mathrm{w}}^{\mathrm{b}}$ and $p_{\mathrm{w}}^{\mathrm{t}}$ are the water pressures at the bottom and top sides of the discontinuity.

The longitudinal hydraulic coefficient $t^{\mathrm{l}}$ is estimated using the Reynolds lubrication equation, which describes the laminar flow of an incompressible and Newtonian fluid flowing between two parallel plates (Zimmerman and Yeo, 2000). It reads:

$$t^{\mathrm{l}} = \frac{r_{\mathrm{n}}^3}{12} + t_0^{\mathrm{l}} \tag{15}$$

where $r_{\mathrm{n}}$ [m] is the normal separation of the interface, and $t_0^{\mathrm{l}}$ [m$^3$] is the initial longitudinal hydraulic coefficient, which makes it possible to assign an initial longitudinal transmissivity to the discontinuity even if it is closed from the mechanical point of view. The longitudinal hydraulic coefficient $t^{\mathrm{l}}$, defined in Eq. (11), plays a similar role as the intrinsic permeability $K$ in the equation governing fluid flow in the continuum. Both parameters account only for the geometrical characteristics of the medium through which the liquid flows, i.e., they are independent of the fluid properties. The fluid properties (as well as the time dimension) are introduced via the water dynamic viscosity $\mu_w$ in Eqs. (2) and (9), for the continuum and discontinuities, respectively.

The width $w$ will evolve with the normal separation of interface $r_{\mathrm{n}}$:

$$w = r_{\mathrm{n}} + w_0 \tag{16}$$

where $w_0$ [m] can be set to be non-zero to assign an initial storage volume to the discontinuity even if it is mechanically closed (Liaudat et al., 2023).

#### 2.3.2. Mechanical problem

The balance of momentum for the interface element reads:

$$\frac{\partial \boldsymbol{\sigma}_{\mathrm{c}}}{\partial l} = \mathbf{0} \tag{17}$$

where $l$ is the longitudinal axis of the interface element, and $\boldsymbol{\sigma}_{\mathrm{c}} = [\sigma_{\mathrm{n}}, \sigma_{\mathrm{l}}]$ [Pa] is the total stress on the interface mid-plane, with $\sigma_{\mathrm{n}}$ and $\sigma_{\mathrm{l}}$ being the normal and shear stress components on that plane. This paper focuses on mode I fracturing. The shear stress component is therefore not discussed here.

For the mechanical constitutive behaviour of the discontinuity, the bilinear traction–separation law schematically depicted in Fig. 2 is used (Mi et al., 1998; Liaudat et al., 2023). More advanced constitutive laws can be incorporated easily into the code. This bilinear law can describe the behaviour of fractures using six parameters: the maximum tension and shear strengths, $\sigma_{\mathrm{n0}}$ [Pa] and $\sigma_{\mathrm{l0}}$ [Pa], the normal and shear "cracking" separation, $r_{\mathrm{n0}}$ [m] and $r_{\mathrm{l0}}$ [m], and the normal and shear debonding separations, $r_{\mathrm{nc}}$ [m] and $r_{\mathrm{lc}}$ [m].

Upon loading, the normal and shear stresses are given by:

$$\sigma_{\mathrm{n}}' = \begin{cases} (1-D)\,K_{\mathrm{nm}} r_{\mathrm{n}} & \text{if } r_{\mathrm{n}} \geq 0 \\ K_{\mathrm{n0}} r_{\mathrm{n}} & \text{if } r_{\mathrm{n}} \leq 0 \end{cases} \tag{18}$$

$$\sigma_{\mathrm{l}} = (1-D)\,K_{\mathrm{l0}} r_{\mathrm{l}} \tag{19}$$

where $\sigma_{\mathrm{n}}'$ [Pa] represents Terzaghi's effective normal stress, defined as $\sigma_{\mathrm{n}}' = \sigma_{\mathrm{n}} + p_{\mathrm{w}}^{m}$, and $K_{\mathrm{n0}} = \sigma_{\mathrm{n0}}/r_{\mathrm{n0}}$ [Pa/m] is the initial normal slope $K_{\mathrm{nm}} = \sigma_{\mathrm{nm}}/r_{\mathrm{n0}}$ is the normal stiffness after $m$th cycles and $\sigma_{\mathrm{nm}} = (1-D_{\mathrm{f}})\sigma_{\mathrm{n0}}$. $D_{\mathrm{f}}$ is the fatigue damage variable and will be defined later. $\sigma_{\mathrm{l}}$ and $r_{\mathrm{l}}$ are the tangential stress and separation respectively, and $K_{\mathrm{l0}} = \sigma_{\mathrm{l0}}/r_{\mathrm{l0}}$ is the tangential slope. (Note that the friction is not included in the shear branch.) When an interface element is used to represent natural fractures, the normal slope can have a physical meaning, interpreted as fracture stiffness, for instance, as a result of interpenetration of fracture surfaces due to presence of asperities (Cerfontaine et al., 2015; Lei and Barton, 2022). In the context of this paper, $K_{\mathrm{n0}}$ is interpreted as penalty coefficients, thus allowing negligible interpenetration of fracture surfaces regardless of their roughness (Cerfontaine et al., 2015). To enforce the contact constraints, the slope should be set high enough to reduce artificial compliance (Liaudat et al., 2023). However, the choice of their values is a trade-off between having artificial compliance and having numerical convergence problems. Additionally, $D$ is the damage variable ranging from 0 (intact rock) to 1 (fully separated fracture). This damage variable evolves as follows:

$$D = \min\left(\frac{\bar{\omega}}{1+\bar{\omega}}\frac{1}{\eta}, 1\right) \tag{20}$$

$$\bar{\omega} = \max(\omega) \tag{21}$$

$$\omega = \left\langle \left(\frac{\langle r_{\mathrm{n}} \rangle}{r_{\mathrm{n0}}}\right)^{\beta} + \left(\frac{|r_{\mathrm{l}}|}{r_{\mathrm{l0}}}\right)^{1/\beta} - 1 \right\rangle \tag{22}$$

$$\eta = 1 - \frac{r_{\mathrm{n0}}}{r_{\mathrm{nc}}} = 1 - \frac{r_{\mathrm{l0}}}{r_{\mathrm{lc}}} \tag{23}$$

where $\omega$ is a positive scalar that defines the mechanical degradation of the interface element for a given normal separations, $\bar{\omega}$ is a history variable that stores the maximum value reached by $\omega$ during the loading history, and $\langle\cdot\rangle = (\cdot + |\cdot|)/2$ is the Macaulay bracket (Liaudat et al., 2023). $\beta$ is a material parameter that characterise the mixed mode damage and is assumed to be 1 in this work (Liaudat et al., 2023). The above equations state that if the separation $r_{\mathrm{n}}$ is less than the normal crack separation $r_{\mathrm{n0}}$, the damage variable $D$ is then zero. If $r_{\mathrm{n0}} < r_{\mathrm{n}} < r_{\mathrm{nc}}$, $D$ is between 0 and 1, determined by the ratio of $(r_{\mathrm{n}} - r_{\mathrm{n0}})/(r_{\mathrm{nc}} - r_{\mathrm{n0}})$. Otherwise if $r_{\mathrm{n}}$ is beyond the debonding separation $r_{\mathrm{nc}}$, $D$ is forced to be 1, indicating a completely separation of the interface element.

To determine the fatigue damage variable, a linear strength degradation is assumed (Xi et al., 2021; Nojavan et al., 2016b). Thus, when

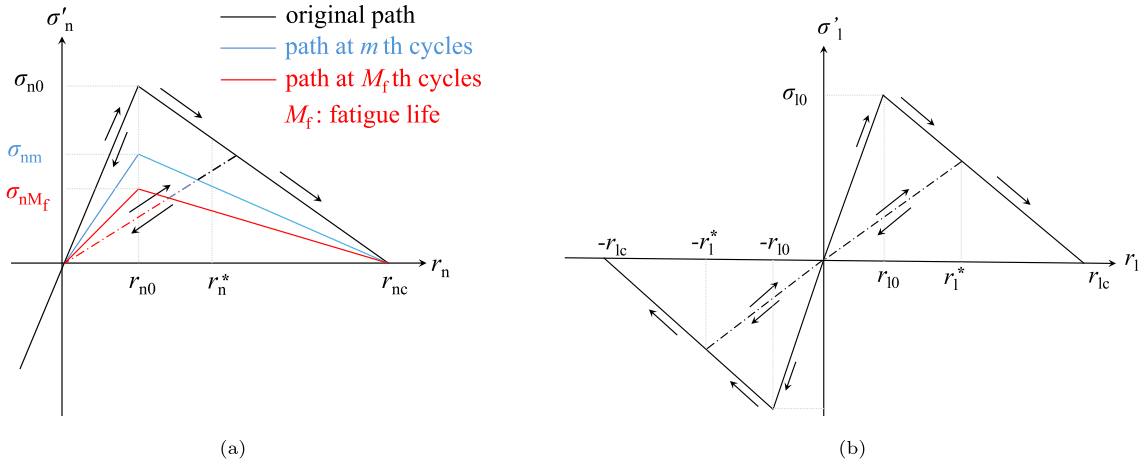


**Fig. 2.** The elasto-damage law. (a) Tensile branch incorporating the fatigue damage; (b) Shear branch.

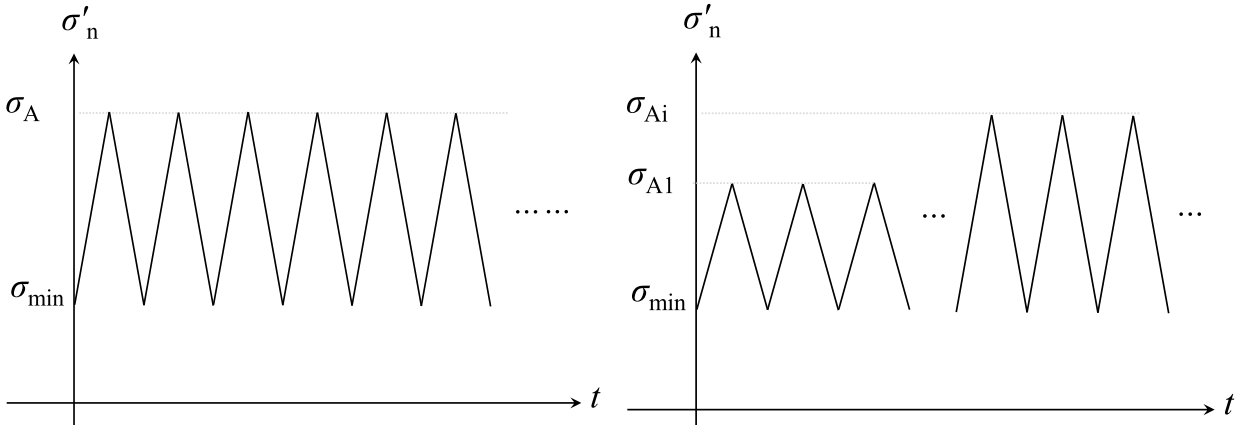


(a) Cyclic loading with constant amplitude.

(b) Cyclic loading with varying amplitude.

**Fig. 3.** Different loading scenarios.

subjected to constant-amplitude cyclic loading (Fig. 3(a)), it is defined as:

$$D_f = \left(1 - \frac{\sigma'_A}{\sigma_{n0}}\right)\frac{m}{M_f} \tag{24}$$

where $\sigma'_A$ [Pa] is the amplitude of the cyclic loading (effective stress). $M_f$ is the fatigue life (maximum number of cycles until failure) under a specific constant-amplitude cyclic loading.

When subjected to varying-amplitude cyclic loading shown in (Fig. 3(b)), Eq. (24) can be further developed based on the Palmgren-Miner's rule, which reads:

$$D_f = \sum_i \left(1 - \frac{\sigma'_{Ai}}{\sigma_{n0}}\right)\frac{1}{M_{fi}} \tag{25}$$

where $i$ indicates the $i$th cyclic loading that has a maximum amplitude of $\sigma'_{Ai}$, as shown in Fig. 3(b). $M_{fi}$ is the fatigue life corresponding to the applied loading level $\sigma'_{Ai}$.

An empirical S–N relationship is used as a criterion to determine the fatigue life $M_{fi}$, which relates the maximum value of the cyclic loading ($\sigma'_{Ai}$) to the fatigue life $M_{fi}$ of the rock. This relationship has been widely used in metals, concrete, and rocks (Nojavan et al., 2016b; Chen et al., 2017; Cerfontaine and Collin, 2018; Xi et al., 2021). It reads (Cerfontaine and Collin, 2018; Xi et al., 2021):

$$\frac{\sigma'_{Ai}}{\sigma_{n0}} = a\log_{10} M_{fi} + b \tag{26}$$

where $a$ and $b$ are model parameters that can be determined from experimental data.

Moreover, mechanical viscosity is added to the contact stress to resolve the solution jump that can result in numerical divergence (Lequesne, 2009; Liaudat et al., 2023):

$$\sigma'_n = \sigma_n + p_w^m + \sigma_v \qquad \text{with} \quad \sigma_v = \zeta\frac{\partial r_n}{\partial t} \tag{27}$$

where $\zeta$ [Pa s/m] is the viscosity added to resolve large fast changes in the solution, which occur faster than the time discretisation, and can cause numerical divergence. The added viscosity $\zeta$ slows down the strain rate and thus stabilised the solution. Detailed discussion on the solution jumps and how the added viscosity helps mitigate this issue can be found in other works (Lequesne, 2009; Liaudat et al., 2023).

### 2.3.3. Thermal problem

The conservation of energy, in terms of temperature, applied to a differential volume of discontinuity $wdl$ reads:

$$\frac{\partial}{\partial t}(w\rho_w c_{pw} T^m) + \frac{\partial q_T^l}{\partial l} - q_T^b - q_T^t = 0 \tag{28}$$

where $q_T^s$ [J/(m$^2$ s)] is the rate of change of the heat stored in the discontinuity, $q_T^l$ [J/(m s)] is the longitudinal heat flow, $q_T^b$ [J/(m$^2$ s)] and $q_T^t$ [J/(m$^2$ s)] are the normal heat flows incoming from the surrounding continuum medium via bottom and top faces to the discontinuity, respectively.

The terms in Eq. (28) can be expanded as:

$$q_{\mathrm{T}}^{\mathrm{l}} = -w\lambda_{\mathrm{w}}\frac{\partial T^{\mathrm{m}}}{\partial l} + c_{\mathrm{pw}}q_{\mathrm{w}}^{\mathrm{l}}T^{\mathrm{m}} \tag{29}$$

$$q_{\mathrm{T}}^{\mathrm{b}} = -\lambda_{\mathrm{w}}\frac{2\breve{T}^{\mathrm{b}}}{\max(w,\bar{w})} + c_{\mathrm{pw}}q_{\mathrm{w}}^{\mathrm{b}}\breve{T}^{\mathrm{b}} \tag{30}$$

$$q_{\mathrm{T}}^{\mathrm{t}} = -\lambda_{\mathrm{w}}\frac{2\breve{T}^{\mathrm{t}}}{\max(w,\bar{w})} + c_{\mathrm{pw}}q_{\mathrm{w}}^{\mathrm{t}}\breve{T}^{\mathrm{t}} \tag{31}$$

where $\breve{T}^{\mathrm{b}} = T^{\mathrm{m}} - T^{\mathrm{b}}$ and $\breve{T}^{\mathrm{t}} = T^{\mathrm{m}} - T^{\mathrm{t}}$ are the temperature jumps between the bottom or top face and the mid-plane, with $T^{\mathrm{m}}$, $T^{\mathrm{b}}$ and $T^{\mathrm{t}}$ being the temperatures at the mid-plane, bottom and top face of interface element, respectively, and $\lambda_{\mathrm{w}}$ is the thermal conductivity of the water. $\bar{w}$ is a penalty coefficient to avoid singularity when interface elements are used to provide potential cracking paths in intact rock. The penalty coefficient should be as small as possible to reduce the artificial compliance.

## 3. Validation against cyclic Brazilian tests

The formulation and numerical implementation (without fatigue) has been previous verified for thermo-hydraulic behaviour (using Lauwerier's problem) and for hydro-mechanical problem (the KGD model) for the combined continuum element and interface elements approach (Luo et al., 2025). In addition, a verification between using only continuum elements and the combined continuum / interface elements approach for intact material, i.e. prior to fracturing occurring, was successful when the interfaces were given a high stiffness. In this section, the proposed method is validated against cyclic Brazilian tests conducted by Erarslan and Williams (2012).

### 3.1. Description of the experiment

The Brazilian test, also known as the splitting tensile strength test, is a common method to estimate the tensile strength of brittle rocks. In this test, a circular disc is placed between loading platens or curved loading jaws, and diametrically loaded until failure (Fig. 4(a)). Upon loading, a line of equally-distributed tensile stress is induced in the centre of the specimen, as shown in Fig. 4(b). The compressive force applied at failure (defined as the maximum force that the sample can sustain) $F_{\max}$ [N] is used to calculate the tensile strength $\sigma_{\mathrm{n0}}$ [Pa] according to:

$$\sigma_{\mathrm{n0}} = -\frac{2F_{\max}}{\pi d h \alpha}\left(\sin\alpha - \frac{\alpha}{2}\right) \tag{32}$$

where $d$ [m] and $h$ [m] are the radius and the thickness of the disc, respectively, and $\alpha$ is the contact angle between the disc and the curved loading jaw (Navidtehrani et al., 2022).

In the work of Erarslan and Williams (2012), Brisbane tuff was used to produce specimens with a diameter of 52 mm and a thickness of 26 mm. The material properties are presented in Table 1. The tensile strength was obtained using Eq. (32) based on monotonic Brazilian tests. The shear strength is not reported in the original paper (Erarslan and Williams, 2012), but is set high in the following simulations to avoid numerical difficulties resulting from the strong stress concentration at the contact arc. The specimens were used to conduct monotonic and cyclic Brazilian tests in a setup, whose two jaws were designed to make contact with the specimen at diametrically opposed surfaces over an arc of contact of $\alpha = 10°$ (Erarslan and Williams, 2012). The specimens were loaded with monotonic or cyclic loading at a rate of 200 N/s. In the monotonic loading case (in this paper sample BR-3 is taken as an example), the sample failed when the loading reached 20.98 kN. This case will be simulated first to explore the mesh sensitivity. A series of cyclic Brazilian tests with constant amplitude at 95%, 90%, 80% and 70% of $F_{\max}$ (the load at failure under monotonic loading) were performed to determine the fatigue life, with the experimental S–N relation and fitted relationship presented in Fig. 5. The cases of cyclic tests with constant amplitude at 95% and 90% of $F_{\max}$ are then simulated to validate the modelling approach against experimental results, with a special focus on the experimental fatigue life and fracture patterns.

**Table 1**
Material properties and model parameters (Erarslan and Williams, 2012).

| Parameter | Symbol | Value | Unit |
|---|---|---|---|
| Material properties | | | |
| Young's modulus | $E$ | 2.6E10 | Pa |
| Poisson's ratio | $\nu$ | 0.26 | – |
| Mode-I fracture stiffness | $K_{\mathrm{IC}}$ | 1.18E6 | Pa m$^{0.5}$ |
| Tensile strength (BR-3, used for monotonic loading) | $\sigma_{\mathrm{n0}}$ | 9.87E6 | Pa |
| Tensile strength (used for cyclic loading) | $\sigma_{\mathrm{n0}}$ | 10.82E6 | Pa |
| Shear strength | $\sigma_{\mathrm{l0}}$ | 400E6 | Pa |
| Model parameters | | | |
| Cracking separation | $r_{\mathrm{n0}}/r_{\mathrm{l0}}$ | 1E−7/1E−6 | m |
| Debonding separation | $r_{nc}/r_{lc}$ | 1E−5/1E−4 | m |
| Stiffness of interface elements | $K_{\mathrm{n0}}$ | 9.87E13 or 10.82E13 | Pa |
| Mechanical viscosity | $\zeta$ | 1E9 | Pa s/m |
| Parameter $a$ in Eq. (26) | $a$ | −0.051085 | – |
| Parameter $b$ in Eq. (26) | $b$ | 0.9929 | – |

### 3.2. Numerical model

A 2D model is constructed to simulate the monotonic and cyclic Brazilian tests (Fig. 4(b)). The bottom arc with a contact angle of 10° is fixed in both $x$ and $y$ directions, while a distributed monotonic or cyclic load in applied at the top arc. The domain is meshed with second-order triangular elements, and interface elements are inserted between all triangular elements to allow fractures to develop in arbitrary directions. Three different meshes are constructed to investigate mesh sensitivity of the model, as shown in Figs. 6(a) to 6(c). Fig. 6(a) presents a coarse mesh (mesh A, 1770 continuum elements) with a straight line imposed along the central axis of the circle, since a straight fracture is predicted to be induced along the central axis according to analytical solutions (International Society for Rock Mechanics, 1978; Navidtehrani et al., 2022). Interface elements were inserted between all continuum elements. Yet, due to the likely highest tension values along this straight line, it provides a preferential cracking path. In contrast, Figs. 6(b) and 6(c) present a coarse (mesh B, 1484 continuum elements) and a finer mesh (mesh C, 12 268 continuum elements), respectively, without the imposed straight line along the central axis, and interface elements inserted between all continuum elements. Consequently, no cracking path along the central axis is prescribed in the meshes of Figs. 6(b) and 6(c). The model parameters are shown in Table 1. The tensile strength and the debonding separation are determined from material tensile strength and mode-I fracture stiffness. The stiffness of the interface element is set to a high value to reduce artificial compliance while managing numerical convergence.

### 3.3. Numerical simulation of the monotonic Brazilian test

Simulation results of the monotonic Brazilian test on sample BR-3 are discussed here. The loading was applied at a rate of 200 N/S until a maximum load of 20.98 kN was reached, consistent with the experiment. A sensitivity analysis of the mesh is first conducted, with the results shown in Figs. 6(d) to 6(i). In Figs. 6(d) to 6(f), the damage variable $D$ is shown to highlight the simulated fracture patterns at failure for the three meshes. Fig. 6(d) shows that a straight fracture along the central axis is simulated with mesh A, in which a straight line (of interface elements) is imposed along the central axis. This is consistent with the experimental fracture pattern shown in Fig. 7(b)

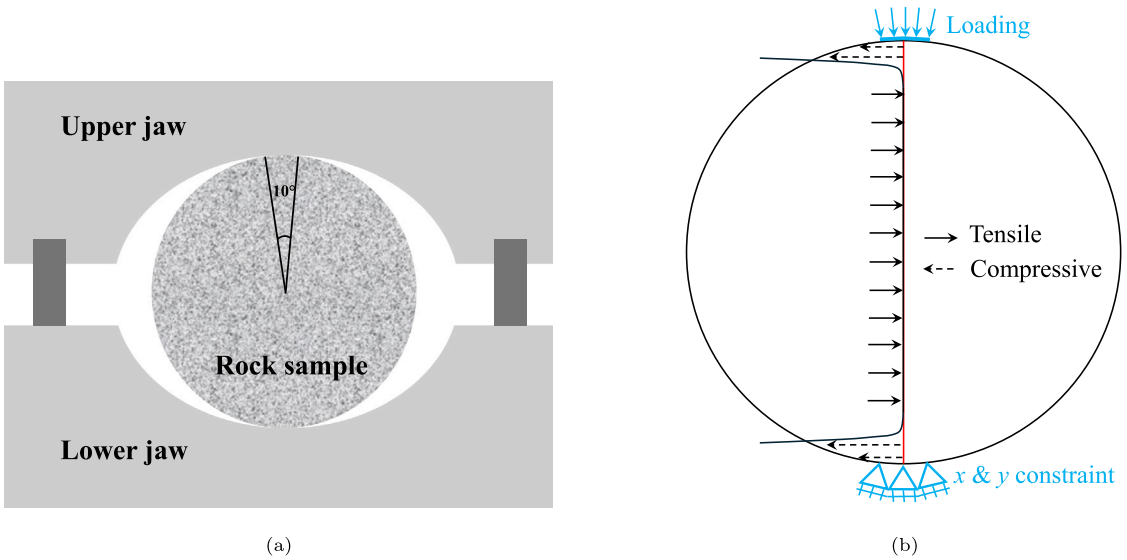


**Fig. 4.** (a) Description of Brazilian test; (b) description of the numerical model, depicting tensile stress distribution along the centre of the disc. Note the interface elements are inserted in-between all the continuum elements to provide arbitrary potential cracking paths.

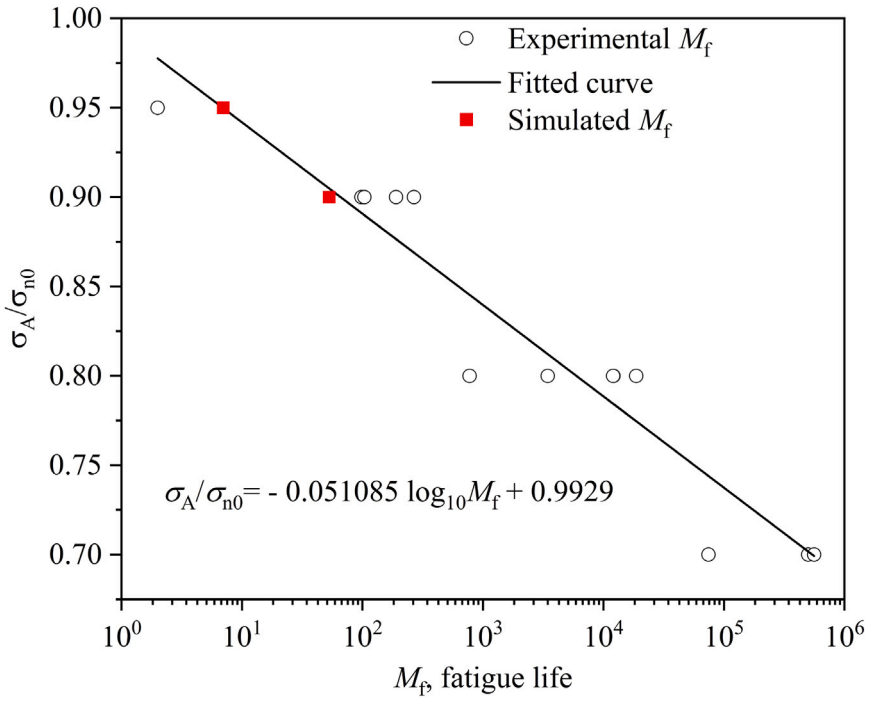


**Fig. 5.** Experiment and simulation results of fatigue life $M_f$ under different maximum loading $\sigma_A$.
*Source:* Experimental data is from Erarslan and Williams (2012).

and the theoretical solution. The loading at failure is 20.98 kN, which corresponds to a tensile strength of 9.87 MPa, showing good agreement with the input tensile strength. Fig. 6(g) presents the corresponding horizontal stress at failure, having a maximum tension of around 7.25 MPa, indicating a relaxation of stress after the tensile fracture occurs.

In contrast, no damage is seen in Fig. 6(e) with mesh B, in which the mesh is coarse and no straight line is imposed along the central axis, and consequently the interface elements in the centre do not orient vertically. In Fig. 6(h) tension of approximately 10 MPa (exceeding the tensile strength) appears along the central axis, thus should induce fractures, but does not due to the mesh orientation. Instead, the fracture can only be induced if the load is increased to 29.12 kN in the simulation using the coarse mesh in Fig. 6(b), almost 40% higher than the 20.98 kN in the experiment. This is because the interface elements in the centre are orientated approximately 30° away from the vertical. Consequently, the tensile stresses on these non-vertical interface elements are less than the maximum tensile stress, which is in the horizontal direction. Although mesh B cannot accurately predict the applied failure loading, it does accurately represent the stress distribution, which allows the mesh to be adjusted for a follow-up analysis. This highlights the impact of allowing fractures which conform only to element edges, illustrating that an iterative simulation approach may be needed to obtain an accurate outcome.

Alternatively, if the mesh in the central part of the model is made sufficiently fine (to automatically generate some straight mesh edges in the central part), as in the mesh C shown in Fig. 6(c), the central

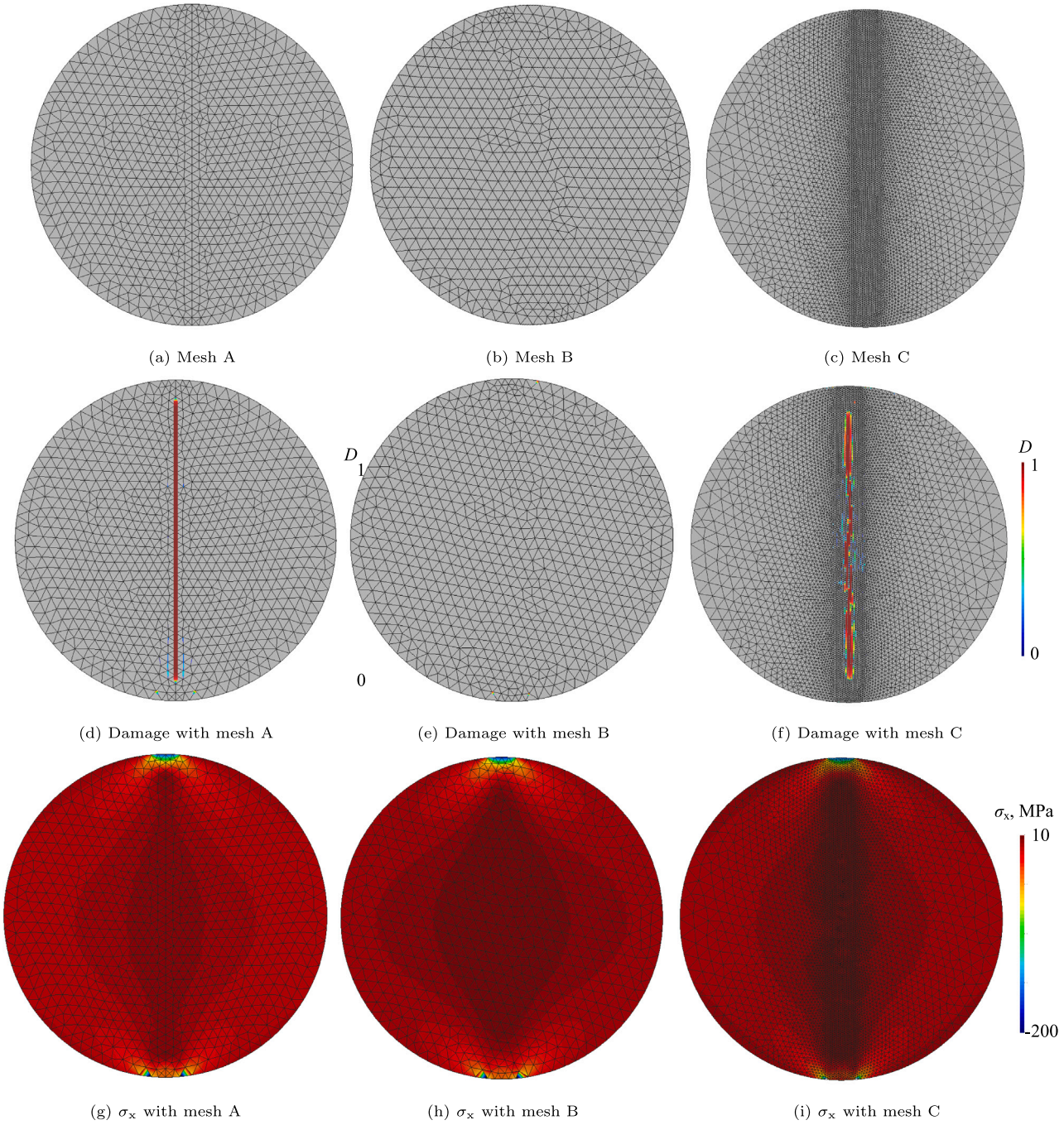


**Fig. 6.** Mesh sensitivity analysis. (a)–(c): three different meshes consisting of second-order triangle continuum elements and interface elements that are inserted between all the continuum elements to provide arbitrary potential cracking paths. (a) Coarse mesh (1770 continuum elements) with a straight line imposed along the central axis of the circle; (b) coarse mesh (1484 continuum elements) without the imposed straight line along the central axis; (c) finer mesh (12 268 continuum elements) without the imposed straight line along the central axis. (d)–(f): Corresponding simulated damage variable under an axial load of 20.98 kN, indicating the fracture patterns. (g)–(i): Distribution of $\sigma_x$ at failure.

fracture can be simulated (Fig. 6(f)), even though the fracture still has to follow the element edges. In Fig. 6(i), $\sigma_x$ is again relaxed along the central axis with a distribution similar to that of Fig. 6(g) as a result of fracture(s) formation. Due to the less structured alignment of the mesh, the fracture distribution is less even and leads to a less even stress distribution immediately around the fracture zone, resulting in a calculated tensile strength of 8.85 MPa. The mesh sensitivity analysis highlights the influence of the mesh orientation and mesh density on the simulation results, although the stresses prior to fracturing are almost identical. A priori knowledge of the position and direction of the maximum tensile stress is therefore helpful when using of coarse mesh, underscoring the importance of the analytical solutions. Otherwise, several different meshes may be used to capture the correct fracture propagation.

Based on the model with mesh presented in Fig. 6(a), a comparison of simulated and experimental axial and lateral strains is presented in Fig. 7(a), showing generally good agreement with a slight deviation, associated with the artificial compliance resulting from insertion of

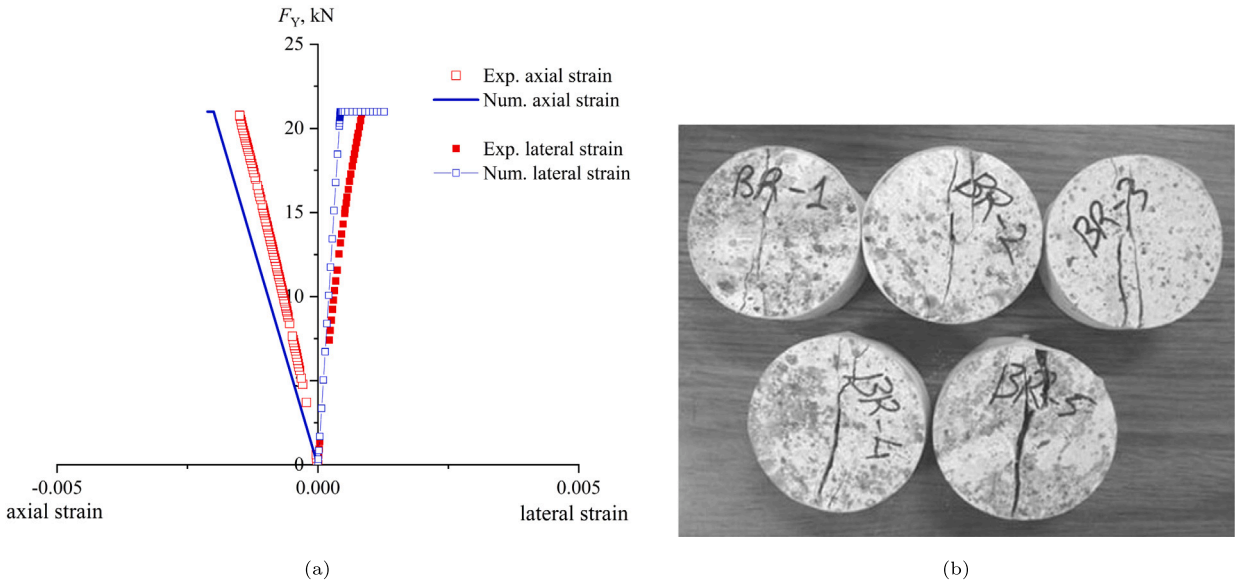


**Fig. 7.** (a) Comparison of experimental and numerical results of axial and lateral strain in the monotonic Brazilian test on sample BR-3. (b) Sample BR-3 after failure under monotonic loading in the experiment.[1]

interface elements. In addition, failure can be clearly seen at the turning point on the simulated curve when loading reaches 20.98 kN, as shown in Fig. 7(a), indicating increasing strain since the specimen failed and could not sustain the controlled loading. The peak loading is reached at time step 104.9 s.

### 3.4. Numerical simulation of the cyclic Brazilian test

A series of cyclic experimental tests with maximum loading at 95%, 90%, 80% and 70% of $F_{max}$ (23 kN) was performed to determine the corresponding fatigue life (Erarslan and Williams, 2012). In this section, the numerical model with the mesh imposed with a straight line along the central axis (Fig. 6(a)) is used to simulate the cyclic Brazilian tests. Based on the element test data shown in Fig. 5, both parameters $a$ and $b$ of the empirical relationship (Eq. (26)) can be determined. In addition, the tensile strength is chosen as 10.87 MPa, as derived from the maximum force applied $F_{max}$ (23 KN). Other material properties and model parameters are kept the same as shown in Table 1. We select the cases where the maximum loading during cyclic loading are 95% and 90% of $F_{max}$ (23kN) as examples to demonstrate the capability of the proposed model.

Figs. 8(a) and 8(c) show the lateral and axial strain evolution with time. It is clearly shown that a sudden sharp increase in lateral strain is observed in the 8th and 54th cycles in the cases of 95% and 90% $\sigma_{max0}$, respectively. As is shown in Fig. 5, the predicted fatigue life is captured by the S–N curve fitted from the experimental data. In addition, as opposed to the single failure observed in monotonic tests, a complex fracture pattern is seen in the experimental results, resulting in an overall failure of the sample (Fig. 9), with the numerical results also indicating a network of fractures. The predicted fatigue life and fracture patterns consistent with the experimental results thereby demonstrate the capability of the proposed method to capture the fatigue damage due to cyclic loading at different loading amplitudes.

To further demonstrate the capability of the proposed model to handle varying-amplitude cyclic loading, two synthetic loading cases (not performed experimentally) with varying-amplitude cyclic loading are simulated. In Case A, the applied maximum load is equal to 90% $\sigma_{max0}$ for the first 10 cycles, before increasing to 95% $\sigma_{max0}$ in the later cycles (Fig. 10(a)). The corresponding results (Fig. 10(b)) show that failure of the sample happens at the 15th cycle, less than the fatigue life (54 cycles) under cyclic loading with constant maximum loading at 90% $\sigma_{max0}$ but more than that (8 cycles) under cyclic loading with constant maximum loading at 95%$\sigma_{max0}$. Inspired by the results from Case A, the applied maximum load in Case B is set to 95% $\sigma_{max0}$ in the first 5 cycles, before decreasing to 90%$\sigma_{max0}$ in later cycles (Fig. 10(c)). Interestingly, unlike Case A where failure happens after 14 cycles (first 10 lower-amplitude cyclic loading + later 4 higher-amplitude cyclic loading), failure is seen in the 31st cycle in Case B (Fig. 10(d)).

## 4. Validation against cyclic hydraulic fracturing test

### 4.1. Description of the experiment

The hydraulic fracturing test is widely used to determine the tensile strength of rocks and/or the magnitude of the in situ stresses. Zhuang et al. (2019) conducted laboratory (cyclic) hydraulic fracturing tests on granite samples cored from the Pocheon geothermal field to demonstrate the concept of cyclic stimulation. The targeted Pocheon granite contained three orthogonal cleavage planes, namely the rift (R), grain (G) and hardway (H) planes. Specimens used in the experiments were cored perpendicular to each of the R, G and H planes, and thus are labelled as R, G and H groups, respectively. The rift plane was seen to have the weakest strength, with an average measured Brazilian tensile strength equal to 6.1 MPa. Hydraulic fracturing tests on specimens in Group G and H were seen to induce fractures in the weakest rift plane. In this paper, we focus only on the fracturing tests on specimens from group H, with the orientation of the sample and the cleavage planes shown in Fig. 11(a). Other properties of the specimens in group H are presented in Table 2.

A borehole with a diameter of 8 mm was drilled through the central axis of the specimens to allow the injection of fluid, as is shown in Fig. 11(a). Two sets of tests were conducted, one using a controlled pressurisation rate and the other with a controlled injection rate. Here, we focus on the tests of controlled injection rate (100 $mm^3/s$), in which the horizontal confining pressure is zero while the vertical stress was 25 MPa to prevent fluid leakage from the top and bottom surfaces. Monotonic fracturing was first implemented using 12 specimens to determine an average monotonic breakdown pressure, which was 6.9 MPa. Cyclic

[1] Reprinted from Erarslan and Williams (2012) with permission from Springer Nature. License No.: 6015260514654.

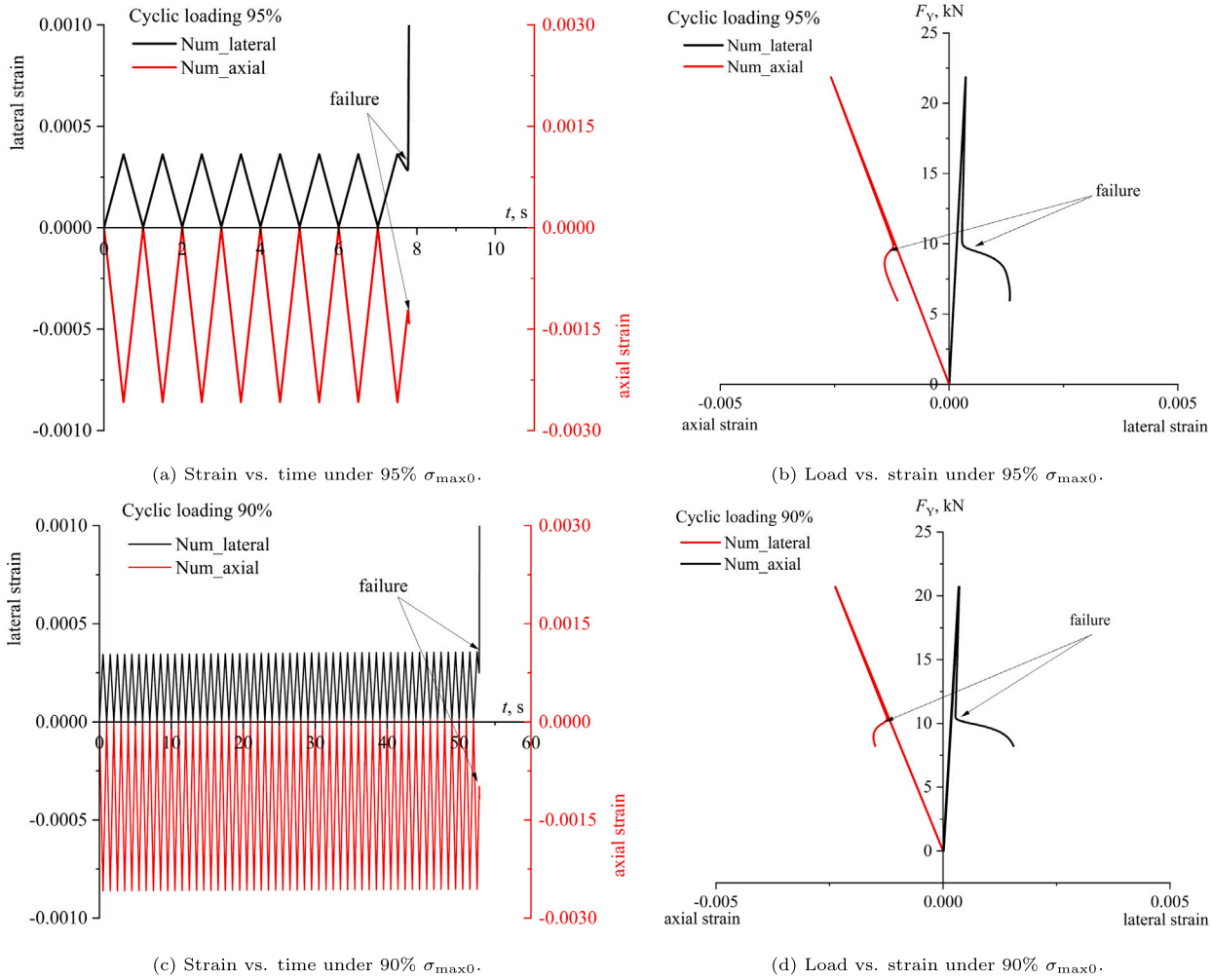


(a) Strain vs. time under 95% $\sigma_{max0}$.

(b) Load vs. strain under 95% $\sigma_{max0}$.

(c) Strain vs. time under 90% $\sigma_{max0}$.

(d) Load vs. strain under 90% $\sigma_{max0}$.

**Fig. 8.** Lateral (positive) and axial (negative) strain evolution with time and loading under different cyclic loadings.

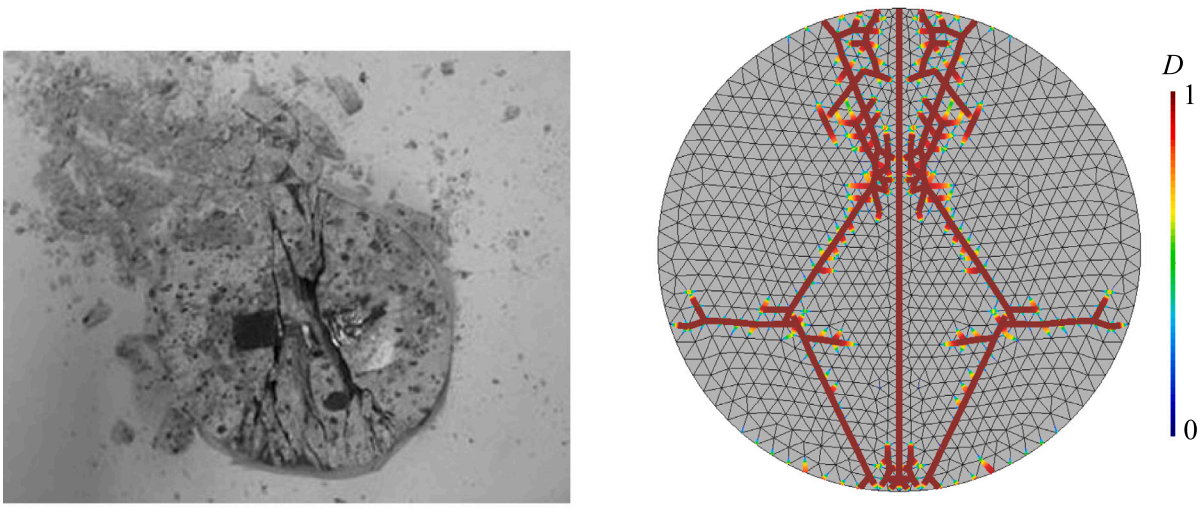


(a) Failed sample under cyclic loading in the experiment.

(b) Failed sample under cyclic loading in the simulation.

**Fig. 9.** Comparison of the failed sample under cyclic loading in the experiment and in the simulation (95% $\sigma_{max0}$). Fig. 9(a): Reprinted from Erarslan and Williams (2012) with permission from Springer Nature. License No.: 6015260514654.

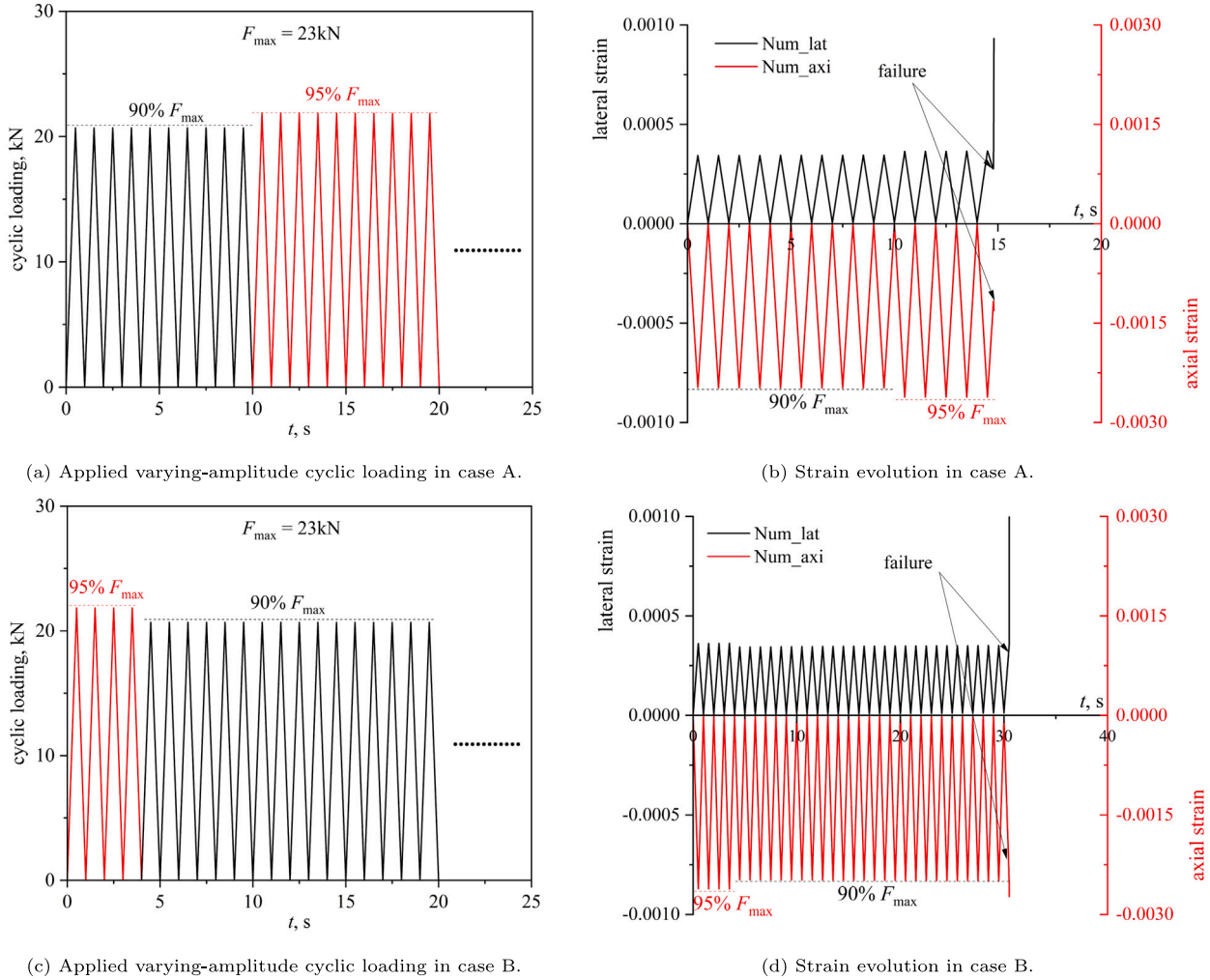


(a) Applied varying-amplitude cyclic loading in case A.

(b) Strain evolution in case A.

(c) Applied varying-amplitude cyclic loading in case B.

(d) Strain evolution in case B.

**Fig. 10.** Simulation results of varying-amplitude cyclic loading and corresponding lateral and axial strain evolution cases.

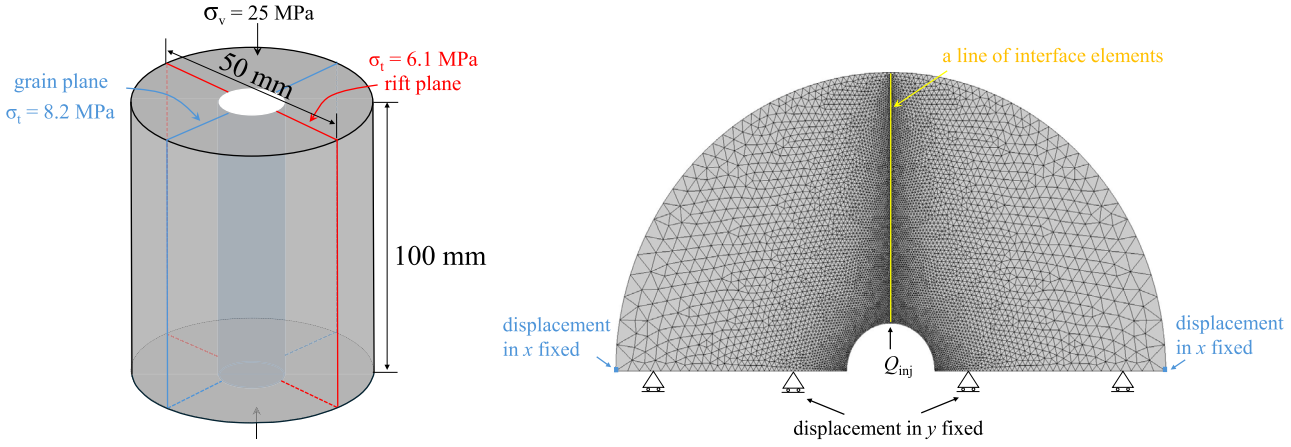


(a) Schematic of the group H samples.

(b) Schematic of the numerical model.

**Fig. 11.** Description of the Pocheon granite specimen in group H and the corresponding numerical model. A line of interface elements is used in the model to represent the weakest rift plane, on which fracture can be induced by injection of fluid.

fracturing tests then followed with a maximum injection pressure ranging from 74% to 95% of the monotonic breakdown pressure, using another 34 samples. Since injection rate was controlled, the injection time was therefore adjusted to achieve the desired injection pressure. Fig. 12 presents the number of cycles needed to fail the specimens under different maximum injection pressure in the experiments. Despite the noticeable scatter in the experimental data, a linear regression in the $\log_{10}$ basis is applied, since this formulation adequately represents the pronounced reduction in strength during the early loading cycles and the fatigue limit identified experimentally (Cerfontaine and Collin,

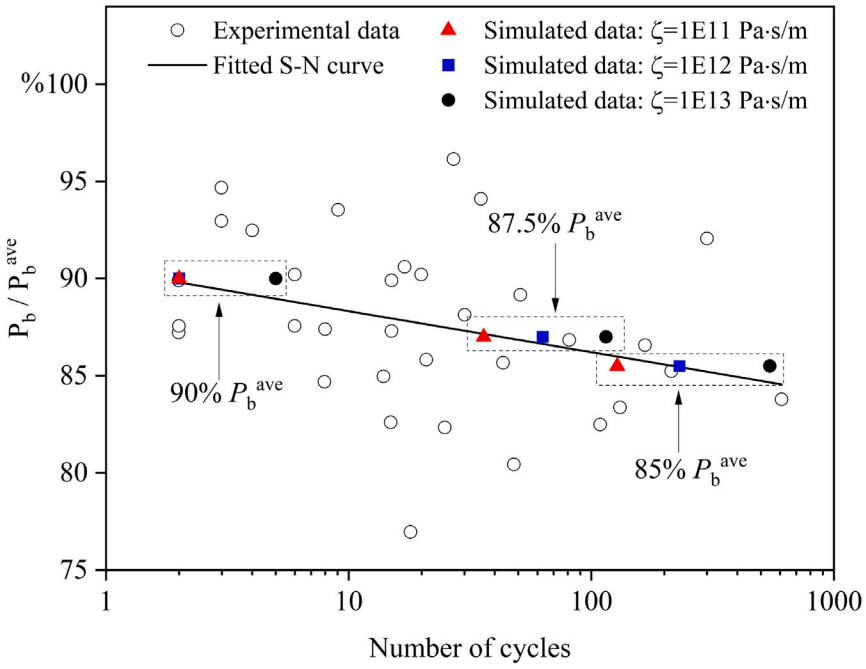


**Fig. 12.** Experiment and simulation results of fatigue life $M_f$ under different maximum injection pressure $p_{inj}$.

**Table 2**
Properties of the Pocheon granite specimens in group H and model parameters.

| Material properties | | | |
|---|---|---|---|
| Parameter | Symbol | Value | Unit |
| Young's modulus | $E$ | 5.8E10 | Pa |
| Poisson's ratio | $\nu$ | 0.30 | – |
| Density | $\rho_s$ | 3000 | kg/m$^3$ |
| Tensile strength (rift plane) | $\sigma_{n0}$ | 6.1E6 | Pa |
| Shear strength (rift plane) | $\sigma_{l0}$ | 192E6 | Pa |
| **Model parameters** | | | |
| Cracking separation | $r_{n0}/r_{l0}$ | 1E−7/1E−6 | m |
| Debonding separation | $r_{nc}/r_{lc}$ | 2E−7/1E−4 | m |
| Mechanical viscosity | $\zeta$ | 1E12 | Pa s/m |
| Parameter $a$ in Eq. (26) | $a$ | −0.021129 | – |
| Parameter $b$ in Eq. (26) | $b$ | 0.90437 | – |

2018). The fitting function results in a standard deviation of 0.043, indicating the function captures the trend generally well. The noticeable scatter in the experimental data reflects the inherent heterogeneity of rock strength and microstructure. The present cohesive zone model employs uniform material parameters and therefore represents an average material response. As such, local variability in strength or stiffness is not explicitly modelled. Incorporating spatially variable or stochastic parameters could further improve the ability of the model to capture experimental scatter and is a next step to be taken.

### 4.2. Numerical model

A 2D model is constructed to simulate both the monotonic and cyclic fracturing tests (Fig. 11(b)). Only half of the horizontal section of the specimen is considered due to symmetric condition. A line of interface elements is inserted along the symmetry axis to represent the weakest rift plane, along which fracture can be induced upon fluid injection. The solid elements represent the rock matrix, which is assumed to be impermeable due to its extremely low permeability. The bottom boundaries of the model are fixed along the $y$ direction, with two nodes at the left and right sides fixed along the $x$ direction to provide reaction to the whole system. No confining stress is applied matching the experimental conditions. Other model input parameters for the interface elements are summarised in Table 2.

### 4.3. Numerical simulation of the monotonic injection tests

Monotonic fracturing is first simulated to demonstrate the capability of the model and determine the simulated monotonic breakdown pressure. A ramped injection rate, shown in Fig. 13(a), is used to simulate the borehole storage effect. Fig. 13 compares the simulation and experimental results of the monotonic hydraulic fracturing test. It shows that the numerical model can successfully capture the pressure response with a peak pressure at 6.48 MPa (compared to 6.9 MPa in the experiment). Additionally, the damage variable of the all of the interface elements is recorded in the simulation and averaged and compared with the AE records of the experiment. Both values represent the damage process of the rock sample in different ways. When the averaged damage variable reaches 1, it indicates the whole line of interface elements is fully opened. The time period over which the damage variable increases from zero to 1 is the same time period with the AE events with the highest amplitude and most densely recorded events.

### 4.4. Simulation results of the cyclic injection tests

The model then is used to simulate the cyclic fracturing tests to validate against the experimental fatigue life, with the maximum injection pressure reaching 90%, 87% and 85% of the simulated $p_b^{ave}$ (6.48 MPa) in each cycle. Each cycle has the same injection rate and time period, so in cases where damage (partially) occurs, the achieved pressure is lower than the initial pressure. The same domain and input parameters are used as in the monotonic simulations.

The simulated pressure response and averaged damage variable under different cyclic injection pressure are presented in Fig. 14. Fig. 14 shows the granite sample fails in the 2nd cycle, 63rd cycle and

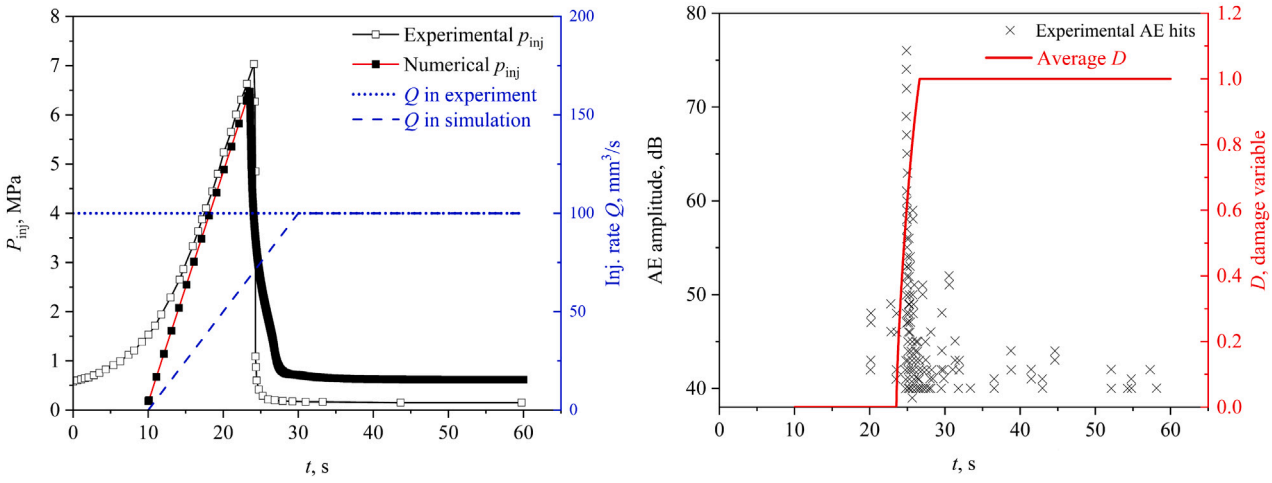


(a) Pressure response.

(b) Experimental AE hits and simulated damage variable $D$.

**Fig. 13.** Comparison of experiment and simulation results of pressure response and damage evolution during monotonic hydraulic fracturing test.

231st cycle under a cyclic injection pressure of 90% $p_b^{mono}$, 87% $p_b^{mono}$ and 85% $p_b^{mono}$ respectively. The relationship between the fatigue life and the cyclic injection pressure is plotted as blue rectangles in Fig. 12, showing a good agreement with the S–N curve fitted from experimental data. Therefore, the proposed model can successfully reproduce the fatigue damage due to cyclic hydraulic stimulation. It should be noted that the domain simulated with the model cannot reproduce the fracture branches observed during the cyclic stimulation experiments, as shown in Fig. 15(b). This is because a single line of zero-thickness interface elements is used to represent the failure plane, while the failure plane(s) in real rock may be more heterogeneous driven by small scale heterogeneities. However, since the fracture branches will most likely restricted within a similar zone due to geometric conditions, a single line of interface elements along this weak plane is reasonably able to capture the main fracture. To be able to simulate the fracture branches, interface elements would need to be inserted in-between all continuum elements with mesh fine enough to capture the pattern, as is done in the simulation of the cyclic Brazilian test.

Viscous stress is added in Eq. (27) to resolve large fast changes in the solution, which occur faster than the time discretisation, and can cause numerical divergence. The added viscosity $\zeta$ slows down the strain rate and thus stabilised the solution, however it could also have an impact on the predicted behaviour including the fatigue life. To investigate the impact of the added viscosity, simulations of the cyclic hydraulic fracturing test are run with four different viscosities, i.e., $\zeta$ = 0 Pa s/m, 1E11 Pa s/m, 1E12 Pa s/m and 1E13 Pa s/m. The predicted fatigue life for different injection pressures with the different viscosities is presented in Fig. 12. It is seen that by increasing the viscosity, the fatigue life also increases. Here, the impact of the viscosity on the results are discussed in detail for the case under $p_{inj} = 90\%\ p_b^{mono}$. The simulated injection pressures are shown in Fig. 16. When adding a mechanical viscosity between 0 and $\zeta$ = 1E12 Pa s/m fracturing occurs in the second cycle and at pressure values of within 1% of each other. However, when the mechanical viscosity is 0 Pa s/m, the simulation cannot converge when interface elements reach the cracking separation $r_{n0}$. If a 1E11 Pa s/m viscosity is added, the divergence problem reduces slightly, but the simulation still diverges after 1.5 cycles. If more viscosity is added, i.e. $\zeta$ = 1E12 Pa s/m or 1E13 Pa s/m, the simulation is able to run continuously, with fatigue life matching the point when the other simulations diverge. However, when adding a larger viscosity, in this case $\zeta = 1E13$ Pa s/m, damage occurs gradually and increases per cycle, with the fatigue life being significantly increased, see Fig. 12. With a further reduction in injection pressure, the differences become larger, however, these are still in fitting with the experimental behaviour and are therefore considered to be reasonable. The value of viscosity which needs to be added is a function of system stiffness and the element size, and therefore needs to be calibrated in a sensitivity procedure for each analysis.

## 5. Validation against cyclic thermo-hydraulic fracturing test

### 5.1. Description of the experiment

Thermal stimulation, which takes advantages of both thermal stress and hydraulic pressurisation, has been proposed and utilised in geothermal reservoirs. This aims to reduce the breakdown pressure during hydraulic fracturing, therefore reducing environmental impacts. Hong et al. experimentally studied the monotonic and cyclic injection of cold liquid nitrogen and water into granite samples (Hong et al., 2023). In this paper, we focus on both monotonic and cyclic injection of cold water conducted by Hong et al. against which the proposed method is validated (Hong et al., 2023).

The samples are formed from granite cored from the province of Shangdong, China, (properties of the granite are presented in Table 3) and were manufactured to be cubes with the size of 100 mm × 100 mm × 100 mm, schematically shown in Fig. 17(a). A hole 60 mm deep and 16 mm in diameter was drilled in the centre of the samples. A steel tube 40 mm deep and 14 mm in diameter was cemented in the hole, leaving a 20 mm deep 'open hole' section. The temperature at the open hole section was monitored by a thermocouple attached to the wall of the open hole.

The experiments consisted of two phases: (1) cooling–heating cycles; (2) fracturing test via injection of cold water. Fig. 18 shows the evolution of the borehole temperature and injection pressure during one single cooling–heating cycle and during the fracturing test respectively. The samples were firstly pre-heated to 473 K in a muffle furnace. Then, the samples were loaded with initial stresses of $\sigma_v$ = 15 MPa, $\sigma_H$ = 10 MPa and $\sigma_h$ = 7 MPa in a true triaxial fracturing equipment (Hong et al., 2023), which is designed to insulate the sample and allows the injection of fluid. In both phases, a 600-second natural cooling down of the samples happened first before any injection of cold water (Stage I in Figs. 18(a) and 18(b)).

In the cooling–heating cycle, shown in Fig. 18(a), water with temperature of 323 K was injected into the borehole with a constant low

[2] Reprinted from Zhuang et al. (2019) with permission from Elsevier. License No.: 6135280240069.

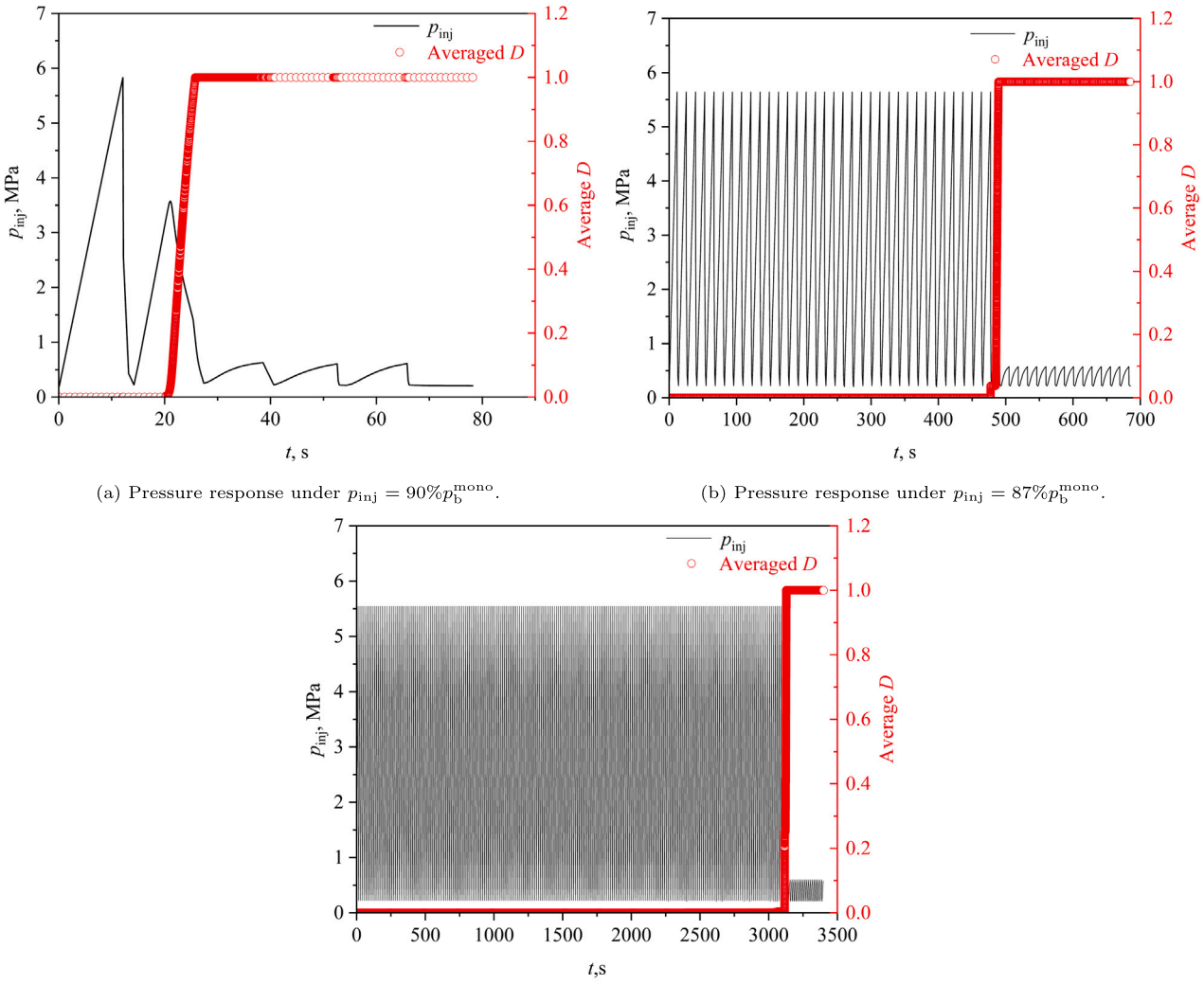


(a) Pressure response under $p_{inj} = 90\%p_b^{mono}$.

(b) Pressure response under $p_{inj} = 87\%p_b^{mono}$.

(c) Pressure response under $p_{inj} = 85\%p_b^{mono}$.

**Fig. 14.** Simulated pressure response and evolution of the average damage variable under different $p_{inj}$.

**Table 3**
Properties of the granite samples and parameters used for the interface elements (Hong et al., 2023).
*Source:* Data from Hong et al. (2023).

| Parameter | Symbol | Value | Unit |
|---|---|---|---|
| Properties of the granite samples | | | |
| Density | $\rho_s$ | 2630 | kg/m$^3$ |
| Young's modulus | $E$ | 39.41 | GPa |
| Poisson's ratio | $\nu$ | 0.28 | – |
| Tensile strength | $\sigma_{n0}$ | 10.02 | MPa |
| Shear strength | $\sigma_{l0}$ | 122 | MPa |
| Permeability | $k$ | 1.1E−3 | mD |
| Porosity | $\phi$ | 0.0045 | – |
| Linear thermal expansion coefficient[a] | $\alpha$ | 4.8E−6 | K$^{-1}$ |
| Thermal conductivity | $\lambda$ | 3.1 | W/(m K) |
| Parameters of the interface elements | | | |
| Cracking separation | $r_{n0}/r_{l0}$ | 1E−8/1E−6 | m |
| Debonding separation | $r_{nc}/r_{lc}$ | 1E−5/1E−4 | m |
| Mechanical viscosity | $\zeta$ | 1E12 | Pa s/m |
| Parameter $a$ in Eq. (26) | $a$ | −1.0 | – |
| Parameter $b$ in Eq. (26) | $b$ | 0.99 | – |

[a] The thermal expansion coefficient is calculated from the thermal expansion coefficient of the dominant minerals' (30% K-feldspar and 47% oligoclase).

injection pressure of 2 MPa, lasting for 180 s (Stage II in Fig. 18(a)). After injection stopped, the open hole naturally re-heated and then cooled (Stage III in Fig. 18(a)). The samples were then removed from the triaxial equipment and re-heated to 473 K in the muffle furnace (Stage IV in Fig. 18(a)) before the next cooling–heating cycle. After the required cooling–heating cycles, the samples were then subjected to high-pressure injection of cold water to determine the (reduced) breakdown pressure, shown in Fig. 18(b). In contrast to the cooling–heating cycle, water with temperature of 323 K was injected into the borehole with a constant injection rate of 30 mm$^3$/min, leading to an average pressurisation rate of 0.386 MPa/s until the breakdown pressure. Four cases were performed by Hong et al. (2023), including monotonic fracturing test without cooling–heating cycle, 1 cycles, 3 cycles and 5 cycles of such cooling and heating, which were labelled as W7, W8, W2 and W9 respectively (Hong et al., 2023). Experimental results show that a decreased breakdown pressure was observed with the number of cooling–heating cycles increasing, as presented in Fig. 19.

### 5.2. Numerical model

A 2D symmetric model, shown in Fig. 17(b), is constructed. Since a single fracture wing was observed in the direction of $\sigma_H$ after fracturing tests in the experiments, only a single line of interface elements are

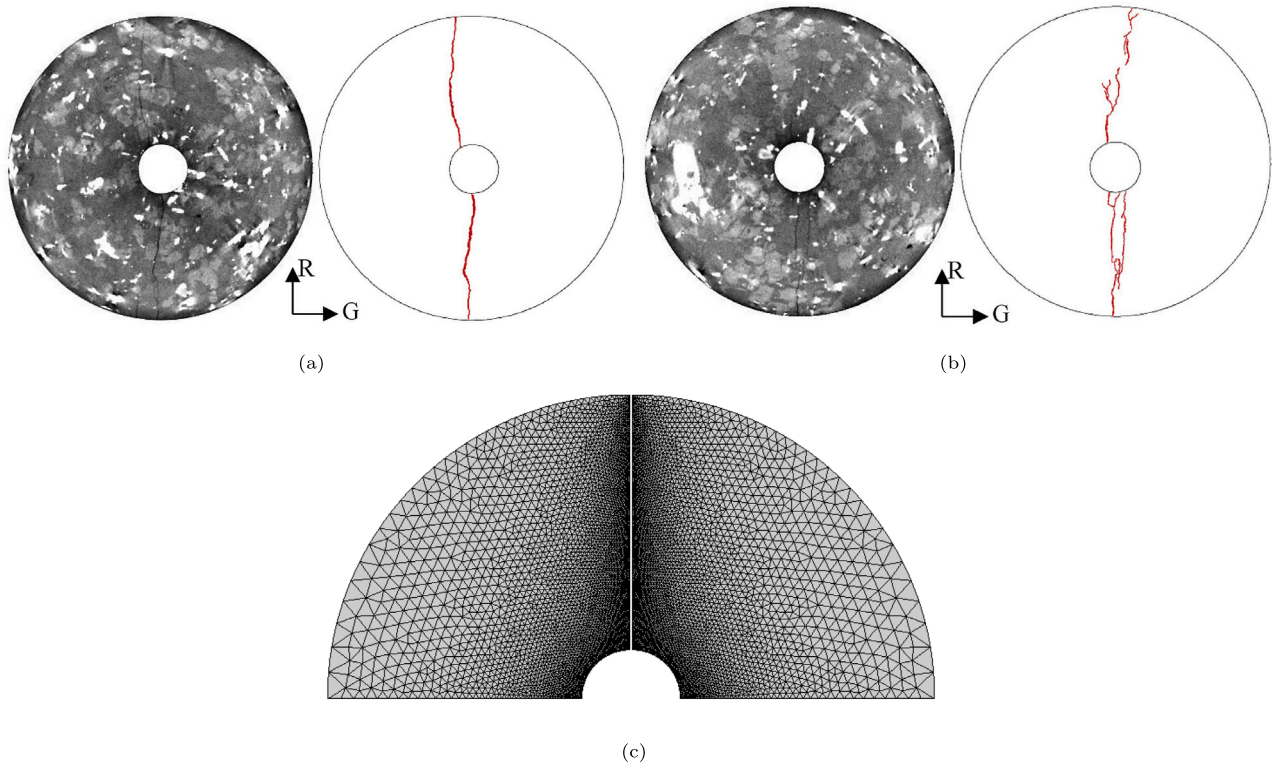


**Fig. 15.** Comparison of fracture pattern in experiments and simulation. (a) Observed fracture pattern in the monotonic stimulation experiment; (b) Observed fracture pattern in the cyclic stimulation (after 65 cycles) experiment; (c) Simulated fracture pattern in the cyclic stimulation (after 63 cycles with the maximum injection pressure reaching 87% of the $p_b^{ave}$). Subfigures (a) and (b) are from Zhuang et al. (2019) with copyright license.[2]

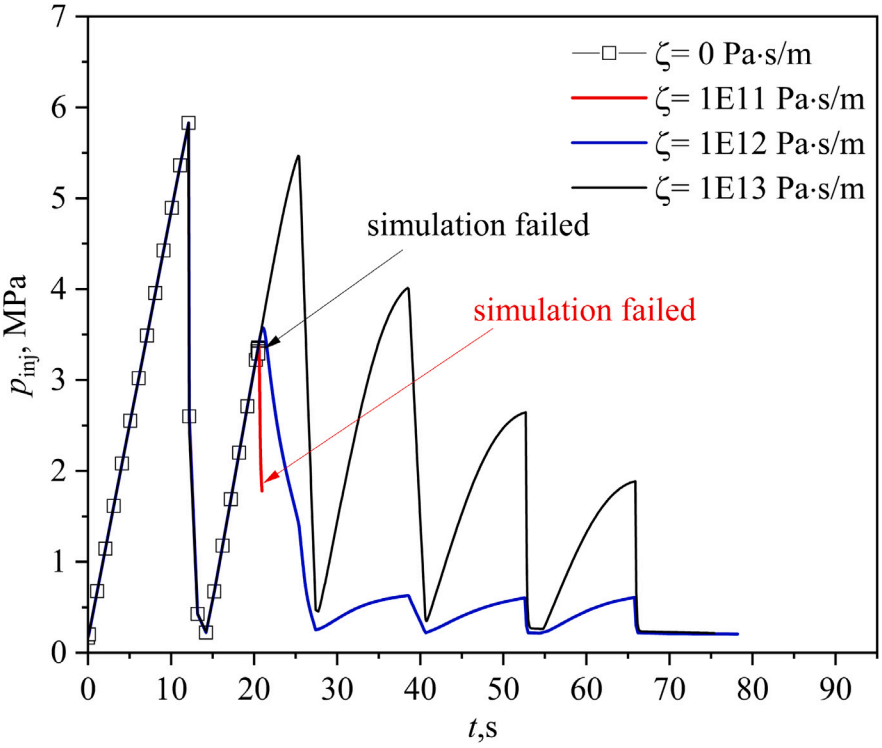


**Fig. 16.** Influence of mechanical viscosity of the fatigue simulation.

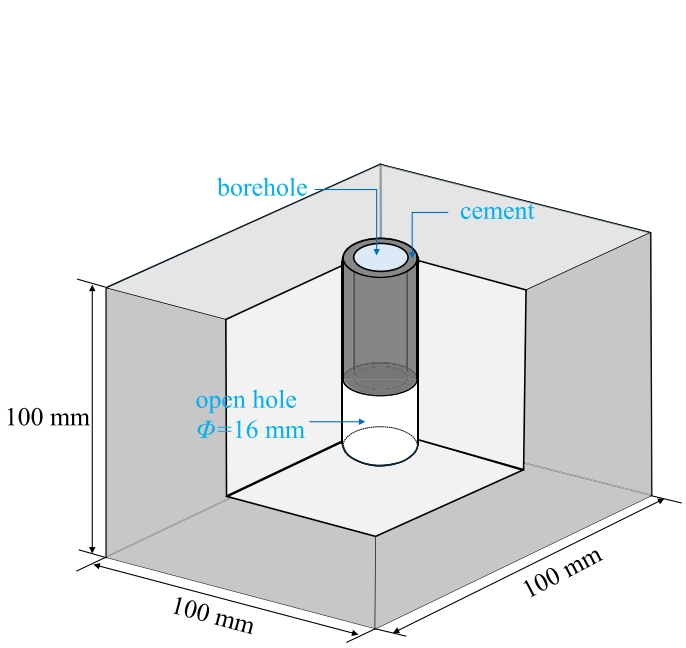


(a) Schematic drawing of the granite sample.

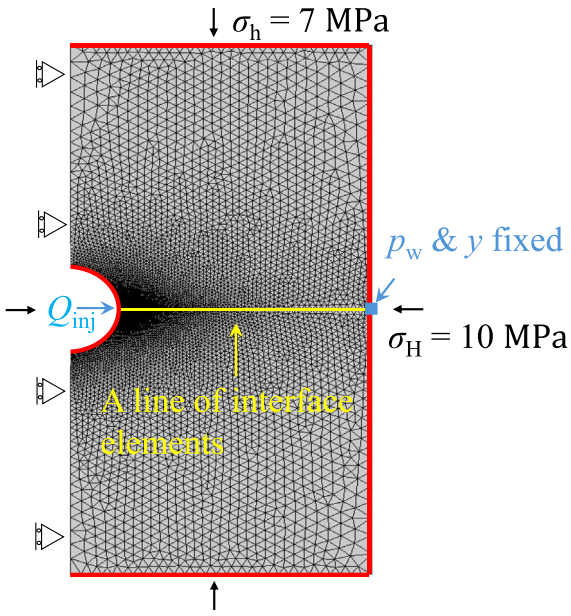


(b) Schematic drawing of the 2D numerical model. Red lines indicate where T is fixed.

**Fig. 17.** Description of the granite samples used in the experiment and the corresponding 2D numerical model. A line of interface elements is used in the model to represent the potential fracture path, on which fracture can be induced by injection of fluid.

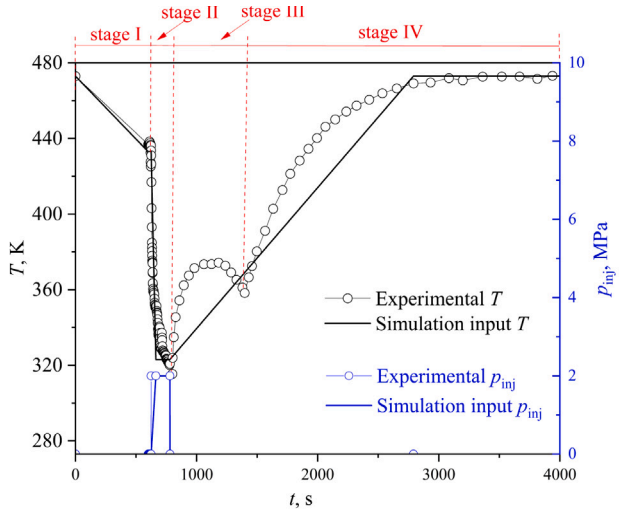


(a) Changes of $T$ and $p_{\mathrm{inj}}$ in one cycle.

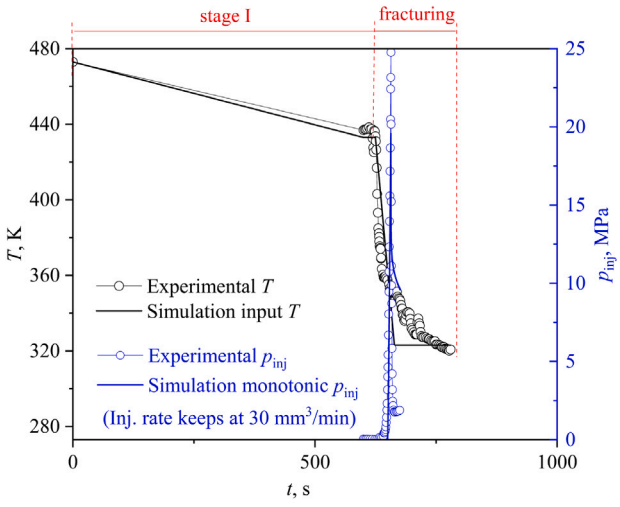


(b) Changes of $T$ and $p_{\mathrm{inj}}$ in fracturing test.

**Fig. 18.** Changes of borehole temperature and injection pressure in (a) one single cooling–heating cycle; and (b) monotonic fracturing test.

inserted the direction of $\sigma_H$ in the model to represent the potential fracture path, which also aids to reduce the computational burden. Initial stresses of $\sigma_{\mathrm{H}}$ = 10 MPa and $\sigma_{\mathrm{h}}$ = 7 MPa are applied. The continuum elements are set to be impermeable due to the extremely low permeability of the granite, but heat conduction is allowed. Water is injected into the interface elements from the mid-node of the interface element at the borehole wall. In Stage II of the cooling–heating cycles, the injection pressure is kept constant at 2 MPa. In contrast, during the fracturing stage, the injection rate is ramped to 30 mm$^3$/min in 60 s and then kept constant. This simulated the storage effect, where in the experiment the pressure build-up rate was an average of 0.386 MPa/s. The temperature at the borehole is controlled based on its evolution shown in Fig. 18.

The key parameters for the interface element are presented in Table 3. Tensile strength was determined via Brazilian test in original paper (Hong et al., 2023). The stiffness is set to a high value to reduce artificial compliance, while the de-bonding separation is estimated from granite toughness. The artificial mechanical viscosity was chosen to be 1E12 Pa s/m based on the sensitivity analysis in Section 4.4 and the similarity in material properties and element size. Since no element tests are available for the samples used in this experiment, the S–N relationship is determined based on the results of the breakdown pressure, shown in Fig. 19. However, since this is a fully THM

**Table 4**
Degraded tensile strengths from the experimental data (obtained by simulating the fracturing test under monotonic injection) and from the simulation considering fatigue damage.

| No. of cycles | Exp. $p_b/p_b^{mono}$, MPa | Exp. $\sigma_{nm}/\sigma_{n0}$, MPa | Simu. $D_f$ | Simu. $\sigma_{nm}/\sigma_{n0}$, MPa |
|---|---|---|---|---|
| 0 | 1 | 1 | 0 | 1 |
| 1 | 0.94 | 0.95 | 0.228 | 0.77 |
| 3 | 0.80 | 0.68 | 0.452 | 0.55 |
| 5 | 0.55 | 0.17 | 0.675 | 0.33 |

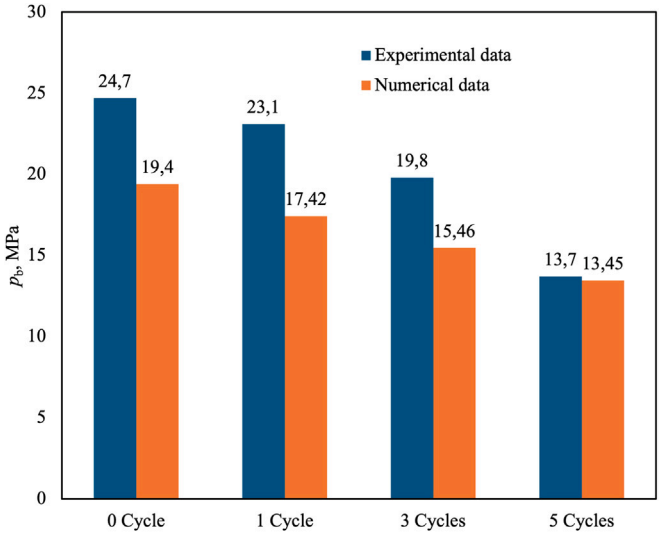


**Fig. 19.** Breakdown pressure in the fracturing tests against the number of cooling–heating cycles and simulations (Hong et al., 2023).

coupled problem, the actual applied normal stress ($\sigma_A$) on the first interface element at the borehole during cooling–heating cycles and the degraded tensile strength ($\sigma_{nm}$) after cycles cannot be obtained directly. First, to determine $\sigma_A$ in Eq. (26), a coupled THM simulation of the cooling stage is performed to determine the largest tangential stress $\sigma_t^{cooling}$ (at the wellbore in the direction of $\sigma_H$) reached during cooling, which is $\sigma_A$. To determine the degraded tensile strength $\sigma_{nm}$, a coupled THM simulation of the fracturing stage with high-pressure injection is performed to determine the tangential stress $\sigma_t^{frac}$ (at the wellbore in the direction of $\sigma_H$). We simulate the monotonic fracturing test, and pick the tangential stresses $\sigma_t^{frac}$ at which the normalised injection pressure (defined as the ratio of the injection pressure to the monotonic breakdown pressure, $p/p_b^{mono}$) reaches the corresponding normalised breakdown pressures ($p_b/p_b^{mono}$) under different cycles in the experiments. These picked tangential stresses $\sigma_t^{frac}$ are viewed as the degraded tensile strengths $\sigma_{nm}$ after different cooling cycles, as is shown in Table 4.

Now we have three data points of different cycles with corresponding degraded tensile strengths under a given normal stress $\sigma_A$ ($\sigma_A$ here is constant since in stage 1 the injection pressure and temperature were not changed.) Based on the expression of $\sigma_{nm}$ (= (1 - $D_f$)$\sigma_{n0}$), (24) and (26), we can determine the corresponding fatigue life $M_f$ of these three cases. Then the parameter $a$ and $b$ can be obtained by best-fitting the three data points.

### 5.3. Results and discussion

Fig. 20(a) presents the normalised injection pressure response during the monotonic fracturing test (i.e. without a cooling–heating cycle) while Fig. 19 compares the exact injection pressure during monotonic fracturing in the experiment and simulation. The simulated monotonic breakdown pressure $p_b$ is 19.5 MPa, around 20% lower than that (24.7 MPa) observed in the experiment. The working hypothesis is that the tensile strength used in the model was taken from the strength measured at room temperature via the Brazilian test (Hong et al., 2023), while the sample was heated to 473 K before conducting the fracturing test. Other possible factors include the chosen values of the linear thermal expansion coefficient $\alpha$ and the thermal conductivity $\lambda$. In the simulation, $\alpha$ is estimated based on the thermal expansion coefficients of the dominant minerals (30% K-feldspar and 47% oligoclase) of the granite used in the experiment (Hong et al., 2023). However, the overall linear thermal expansion coefficient of the rock sample could be different from the one calculated from mineral components. In addition, the thermal conductivity is not mentioned in their paper, and is estimated here. Moreover, due to the limited number of samples tested, sample heterogeneity could play a significant role.

Figs. 20(b), 20(c) and 20(d) shows the normalised pressure response during the fracturing tests after 1, 3 and 5 cooling–heating cycles, respectively. A clear trend of decreasing $p_b$ with increasing number of cycles that was observed in the experiment is well reproduced in the simulation, as is demonstrated in also Fig. 19. The decreased $p_b$ is a result of the fatigue damage accumulated during the cooling–heating cycles, in which both the thermal stress and the 2 MPa injection pressure have an impact. The accumulated fatigue damage and corresponding simulated $\sigma_{nm}/\sigma_{n0}$ are listed in Table 4. The fatigue damage variable $D_f$ increases with increasing number of cooling cycles, contributing to the reduced breakdown pressure. One thing worth explaining is that the values of $\sigma_{nm}/\sigma_{n0}$ after 1 and 3 cycles are lower than their counterparts determined from experimental data, while the value after 5 cycles is higher. This is because the S–N curve is determined by best-fitting for the three data points, leading to an overall least distance to these three points while different differences between the simulated and experimental $\sigma_{nm}/\sigma_{n0}$.

## 6. Conclusions

A new cohesive zone model has been developed to simulate rock fatigue failure under cyclic coupled thermo-hydro-mechanical loading. The model incorporates a fatigue damage variable into the elasto-damage constitutive law that governs the mechanical response of the interface element, which can represent both pre-existing and newly formed fractures. The fatigue damage variable evolves according to the number and magnitude of the cycles, allowing the tensile strength and stiffness of the interface element to progressively degrade. Palmgren-Miner's rule is further integrated to account for varying-amplitude cyclic loading.

The proposed method is validated against three laboratory experiments from the literature that involve different thermo-hydro-mechanical coupling: a cyclic Brazilian test, a cyclic hydraulic fracturing test, and a cyclic thermal stimulation test. In all cases, the model successfully reproduces the observed fatigue damage or the reduction in breakdown pressure associated with cyclic injection or cyclic thermal treatments. A mesh sensitivity analysis indicates that the mesh orientation and density can impact the fracture pattern and simulated rock mass strength. Results improve when stress distributions are known a priori, for example through analytical solutions or by using different meshes. The ability of the method to handle varying-amplitude cyclic loading is demonstrated by the simulation of a synthetic cyclic loading based on the Brazilian test, which shows that fatigue life is shorter when low-amplitude cycles precede high-amplitude cycles than in

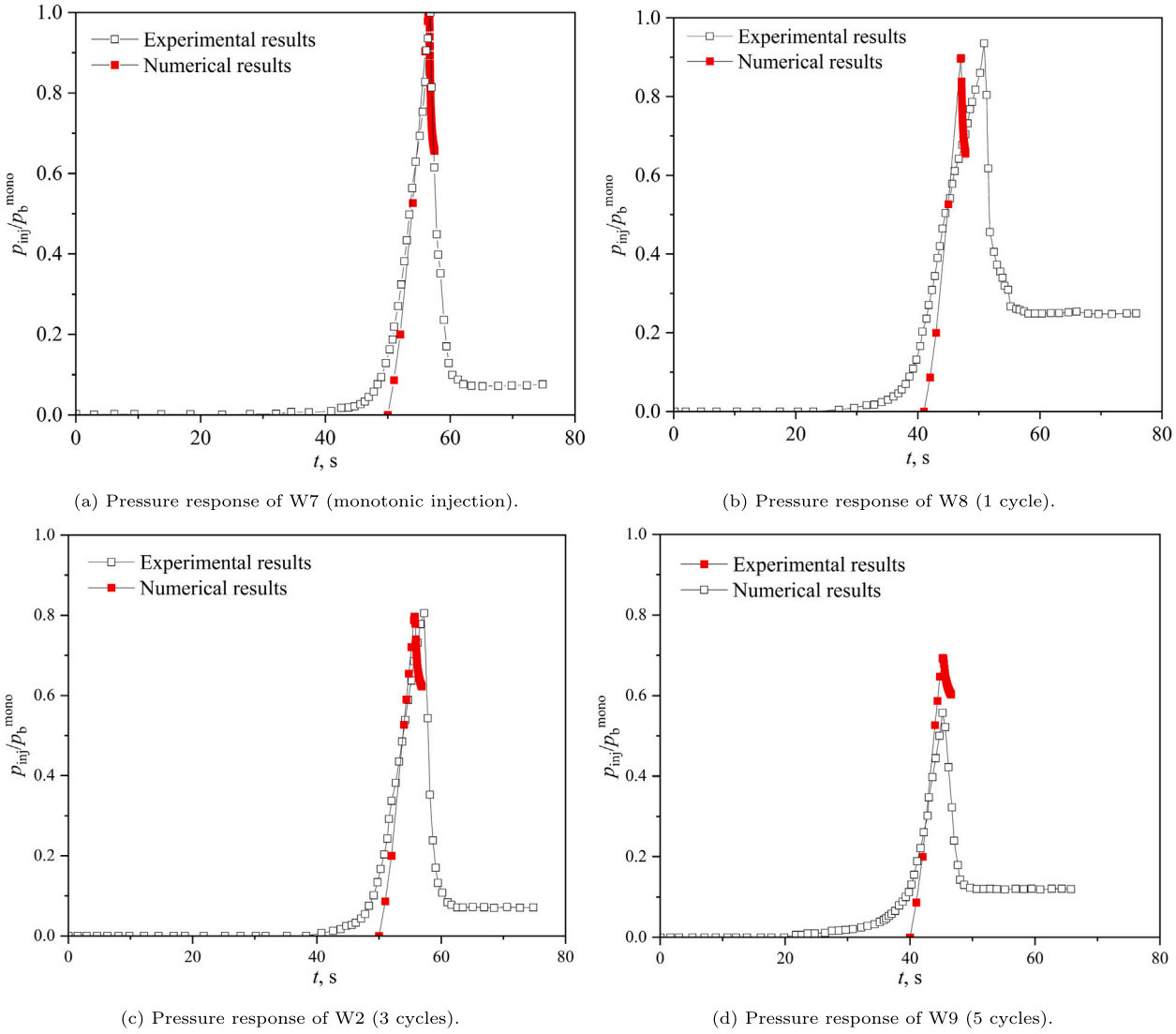


(a) Pressure response of W7 (monotonic injection).

(b) Pressure response of W8 (1 cycle).

(c) Pressure response of W2 (3 cycles).

(d) Pressure response of W9 (5 cycles).

**Fig. 20.** Normalised pressure ($p_b/p_b^{mono}$) response during the fracturing tests of the selected cases W7 (monotonic injection without cooling–heating cycle), W8 (1 cycle), W2 (3 cycles) and W9 (5 cycles) in the experiment and simulation. Note that the simulation is stopped after the breakdown pressure is overcome.

the opposite loading order. Moreover, a sensitivity analysis of the mechanical viscosity, which is added to slow down the strain rate and thus stabilise the numerical solution, shows that increasing the mechanical viscosity can lead to an increasing fatigue life.

The three validation tests confirm the validity of the proposed method to capture the fatigue damage arising from cyclic mechanical, hydro-mechanical, or thermo-hydro-mechanical processes, including cases with varying amplitude. The method can therefore be used to support the design of cyclic thermal stimulation strategy for geo-energy projects, such as geothermal energy production. Extensive experimentation may be needed to determine the fatigue damage variable evolution, and further efforts could be made to determine this more efficiently, e.g. from data collected during field tests.

Finally, cyclic fatigue damage is explicitly included in the present model and is governed solely by the number and magnitude of loading cycles. Creep-induced fatigue (i.e. time-dependent failure under constant sub-critical stress) is not captured, making the model most suitable for stiff and brittle rocks in which creep effects are negligible over the timescale of interest. In addition, the fatigue damage variable currently depends on the peak stress of each cycle rather than on the full stress path. This formulation enables practical calibration for stress paths typical of stimulation campaigns but requires dedicated experiments need to establish the S–N relation when substantially different stress paths are involved. Future efforts to generalise the fatigue damage variable, such as expressing it in terms of the cumulative total strain energy, could reduce this dependence on specific loading scenarios and allow a unified representation of fatigue damage across diverse THM conditions.

## CRediT authorship contribution statement

**Wen Luo:** Writing – review & editing, Writing – original draft, Visualization, Validation, Software, Methodology, Formal analysis, Data curation, Conceptualization. **Anne-Catherine Dieudonné:** Writing – review & editing, Validation, Supervision, Software, Methodology, Formal analysis, Conceptualization. **Josselin Ouf:** Writing – review & editing, Software, Formal analysis. **Florian Amann:** Writing – review & editing, Supervision, Funding acquisition. **Philip J. Vardon:** Writing – review & editing, Validation, Supervision, Project administration, Methodology, Funding acquisition, Formal analysis, Conceptualization.

## Declaration of competing interest

The authors declare the following financial interests/personal relationships which may be considered as potential competing interests:

Given Philip J. Vardon's role as a member of the Editorial Board of Computers and Geotechnics, Philip J. Vardon had no involvement in the peer review of this article and had no access to information regarding its peer review. Full responsibility for the editorial process for this article was delegated to another journal editor. If there are other authors, they declare that they have no known competing financial interests or personal relationships that could have appeared to influence the work reported in this paper.

## Acknowledgements

This project has received funding from the European Union's Horizon 2020 research and innovation programme under the Marie Skłodowska-Curie grant agreement No 956965. Support and help from Joaquín Liaudat throughout this research is gratefully acknowledged.

## Data availability

No data was used for the research described in the article.

## References

Barenblatt, G.I., 1962. The mathematical theory of equilibrium cracks in brittle fracture. Adv. Appl. Mech. 7, 55–129. http://dx.doi.org/10.1016/S0065-2156(08)70121-2.

Cerfontaine, B., Collin, F., 2018. Cyclic and fatigue behaviour of rock materials: Review, interpretation and research perspectives. Rock Mech. Rock Eng. 51 (2), 391–414. http://dx.doi.org/10.1007/s00603-017-1337-5.

Cerfontaine, B., Dieudonné, A.C., Radu, J.P., Collin, F., Charlier, R., 2015. 3D zero-thickness coupled interface finite element: formulation and application. Comput. Geotech. 69, 124–140. http://dx.doi.org/10.1016/j.compgeo.2015.04.016.

Chen, X., Bu, J., Fan, X., Lu, J., Xu, L., 2017. Effect of loading frequency and stress level on low cycle fatigue behavior of plain concrete in direct tension. Constr. Build. Mater. 133, 367–375. http://dx.doi.org/10.1016/j.conbuildmat.2016.12.085.

Choi, H., Park, K., Paulino, G.H., 2020. Mixed-mode fatigue crack growth using cohesive zone modeling. Eng. Fract. Mech. 240, 107234. http://dx.doi.org/10.1016/j.engfracmech.2020.107234.

Collin, F., Li, X.L., Radu, J.P., Charlier, R., 2002. Thermo-hydro-mechanical coupling in clay barriers. Eng. Geol. 64 (2–3), 179–193. http://dx.doi.org/10.1016/S0013-7952(01)00124-7.

De Moura, M.F.S.F., Gonçalves, J.P.M., 2015. Cohesive zone model for high-cycle fatigue of composite bonded joints under mixed-mode I+ II loading. Eng. Fract. Mech. 140, 31–42. http://dx.doi.org/10.1016/j.engfracmech.2015.03.044.

Dugdale, D.S., 1960. Yielding of steel sheets containing slits. J. Mech. Phys. Solids 8 (2), 100–104. http://dx.doi.org/10.1016/0022-5096(60)90013-2.

Erarslan, N., Williams, D.J., 2012. Investigating the effect of cyclic loading on the indirect tensile strength of rocks. Rock Mech. Rock Eng. 45 (3), 327–340. http://dx.doi.org/10.1007/s00603-011-0209-7.

Ewen, J., Thomas, H.R., 1989. Heating unsaturated medium sand. Geotech. 39 (3), 455–470. http://dx.doi.org/10.1680/geot.1989.39.3.455.

Gasc-Barbier, M., Girma, G., Gendre, V., 2014. Laboratory analysis of thermal fatigue in limestone. In: ISRM Regional Symposium - EUROCK 2014. Vigo, Spain, pp. 2014–043, URL: https://onepetro.org/ISRMEUROCK/proceedings-abstract/EUROCK14/EUROCK14/ISRM-EUROCK-2014-043/41646?redirectedFrom=PDF.

Hillerborg, A., Modéer, M., Petersson, P.-E., 1976. Analysis of crack formation and crack growth in concrete by means of fracture mechanics and finite elements. Cem. Concr. Res. 6 (6), 773–781. http://dx.doi.org/10.1016/0008-8846(76)90007-7.

Hofmann, H., Zimmermann, G., Farkas, M., Huenges, E., Zang, A., Leonhardt, M., Kwiatek, G., Martinez-Garzon, P., Bohnhoff, M., Min, K.-B., Fokker, P., Westaway, R., Bethmann, F., Meier, P., Yoon, K.S., Choi, J.W., Lee, T.J., Kim, K.Y., 2019. First field application of cyclic soft stimulation at the pohang enhanced geothermal system site in Korea. Geophys. J. Int. 217 (2), 926–949. http://dx.doi.org/10.1093/gji/ggz058.

Hofmann, H., Zimmermann, G., Huenges, E., Regenspurg, S., Aldaz, S., Milkereit, C., Heimann, S., Dahm, T., Zang, A., Grigoli, F., Karvounis, D., Broccardo, M., Wiemer, S., Hjörleifsdóttir, V., Kristjánsson, B.R., Hersir, G.P., Ásgeirsdóttir, R.u.S., Magnússon, R., Árnadóttir, S., 2021. Soft stimulation treatment of geothermal well RV-43 to meet the growing heat demand of Reykjavik. Geothermics 96, 102146. http://dx.doi.org/10.1016/j.geothermics.2021.102146.

Hong, C.-Y., Yang, R.-Y., Huang, Z.-W., Zhuang, X.-Y., Wen, H.-T., Hu, X.-L., 2023. Enhance liquid nitrogen fracturing performance on hot dry rock by cyclic injection. Pet. Sci. 20 (2), 951–972. http://dx.doi.org/10.1016/j.petsci.2022.07.004.

International Society for Rock Mechanics, 1978. Suggested methods for determining the strength of rock materials in triaxial compression. Int. J. Rock Mech. Min. Sci. Geomech. Abstr. 15 (2), 47–51. http://dx.doi.org/10.1016/0148-9062(78)91677-7.

Jung, S., Diaz, M.B., Kim, K.Y., Hofmann, H., Zimmermann, G., 2021. Fatigue behavior of granite subjected to cyclic hydraulic fracturing and observations on pressure for fracture growth. Rock Mech. Rock Eng. 1–14. http://dx.doi.org/10.1007/s00603-021-02383-5.

Kang, H., Zhang, J., Fan, X., Huang, Z., 2020. Cyclic injection to enhance hydraulic fracturing efficiency: Insights from laboratory experiments. Geofluids 2020, 844293. http://dx.doi.org/10.1155/2020/8844293.

Khoramishad, H., Crocombe, A.D., Katnam, K.B., Ashcroft, I.A., 2010. Predicting fatigue damage in adhesively bonded joints using a cohesive zone model. Int. J. Fatigue 32 (7), 1146–1158. http://dx.doi.org/10.1016/j.ijfatigue.2009.12.013.

Lei, Q., Barton, N., 2022. On the selection of joint constitutive models for geomechanics simulation of fractured rocks. Comput. Geotech. 145, 104707. http://dx.doi.org/10.1016/j.compgeo.2022.104707.

Lequesne, C., 2009. Modeling of Fracture in Heavy Steel Welded Beam-to-Column Connection Submitted to Cyclic Loading by Finite Elements (Ph.D. thesis). Université de Liège, Liège, URL: https://orbi.uliege.be/handle/2268/315091.

Liaudat, J., Dieudonné, A.C., Vardon, P.J., 2023. Modelling gas fracturing in saturated clay samples using triple-node zero-thickness interface elements. Comput. Geotech. 154, 105128. http://dx.doi.org/10.1016/j.compgeo.2022.105128.

Liu, Y., Dai, F., Xu, N., Zhao, T., Feng, P., 2018. Experimental and numerical investigation on the tensile fatigue properties of rocks using the cyclic flattened Brazilian disc method. Soil Dyn. Earthq. Eng. 105, 68–82. http://dx.doi.org/10.1016/j.soildyn.2017.11.025.

Luo, W., Liaudat, J., Ouf, J., Dieudonné, A.-C., Amann, F., Vardon, P.J., 2025. Numerical modelling of fracturing processes during cold water injection into geothermal reservoirs: Verification and qualitative validation. Comput. Geotech. 183, 107186. http://dx.doi.org/10.1016/j.compgeo.2025.107186.

Maiti, S., Geubelle, P.H., 2005. A cohesive model for fatigue failure of polymers. Eng. Fract. Mech. 72 (5), 691–708. http://dx.doi.org/10.1016/j.engfracmech.2004.06.005.

Meng, X., Liu, Y., Ning, Z., Dong, J., Liang, G., Wang, Y., 2023. Fatigue performance of hydraulic asphalt concrete under uniaxial constant-amplitude tensile cycle loading. J. Build. Eng. 80, 108070. http://dx.doi.org/10.1016/j.jobe.2023.108070.

Mi, Y., Crisfield, M.A., Davies, G.A.O., Hellweg, H.B., 1998. Progressive delamination uing interface elements. J. Compos. Mater. 32 (14), 1246–1272. http://dx.doi.org/10.1177/002199839803201401.

Munoz, J.J., Galvanetto, U., Robinson, P., 2006. On the numerical simulation of fatigue driven delamination with interface elements. Int. J. Fatigue 28 (10), 1136–1146. http://dx.doi.org/10.1016/j.ijfatigue.2006.02.003.

Navidtehrani, Y., Betegón, C., Zimmerman, R.W., Martínez-Pañeda, E., 2022. Griffith-based analysis of crack initiation location in a Brazilian test. Int. J. Rock Mech. Min. Sci. 159, 105227. http://dx.doi.org/10.1016/j.ijrmms.2022.105227.

Niu, Y., Wang, G., Wang, J., Liu, X., Zhang, R., Qiao, J., Zhang, J., 2023. Experimental study on thermal fatigue damage and failure mechanisms of basalt exposed to high-temperature treatments. Fatigue Fract. Eng. Mater. Struct. 46 (8), 2909–2928. http://dx.doi.org/10.1111/ffe.14052.

Nojavan, S., Schesser, D., Yang, Q.D., 2016a. A two-dimensional in situ fatigue cohesive zone model for crack propagation in composites under cyclic loading. Int. J. Fatigue 82, 449–461. http://dx.doi.org/10.1016/j.ijfatigue.2015.08.029.

Nojavan, S., Schesser, D., Yang, Q.D., 2016b. An in situ fatigue-CZM for unified crack initiation and propagation in composites under cyclic loading. Compos. Struct. 146, 34–49. http://dx.doi.org/10.1016/j.compstruct.2016.02.060.

Patel, S.M., Sondergeld, C.H., Rai, C.S., 2017. Laboratory studies of hydraulic fracturing by cyclic injection. Int. J. Rock Mech. Min. 95, 8–15. http://dx.doi.org/10.1016/j.ijrmms.2017.03.008.

Robinson, P., Galvanetto, U., Tumino, D., Bellucci, G., Violeau, D., 2005. Numerical simulation of fatigue-driven delamination using interface elements. Internat. J. Numer. Methods Engrg. 63 (13), 1824–1848. http://dx.doi.org/10.1002/nme.1338.

Roe, K.L., Siegmund, T., 2003. An irreversible cohesive zone model for interface fatigue crack growth simulation. Eng. Fract. Mech. 70 (2), 209–232. http://dx.doi.org/10.1016/S0013-7944(02)00034-6.

Scheider, I., 2001. Cohesive model for crack propagation analyses of structures with elastic-plastic material behavior foundations and implementation. URL: https://www.climate-service.info/imperia/md/content/gkss/institut_fuer_werkstoffforschung/wms/czm-doku.pdf.

Turon, A., Costa, J., Camanho, P.P., Dávila, C.G., 2007. Simulation of delamination in composites under high-cycle fatigue. Compos. A 38 (11), 2270–2282. http://dx.doi.org/10.1016/j.compositesa.2006.11.009.

Wei, C., Li, S., Yu, L., Zhang, B., Liu, R., Pan, D., Zhang, F., 2023. Study on mchanism of strength deterioration of rock-like specimen and fracture damage deterioration model under pulse hydraulic fracturing. Rock Mech. Rock Eng. 56 (7), 4959–4973. http://dx.doi.org/10.1007/s00603-023-03313-3.

Xi, X., Yang, S., McDermott, C.I., Shipton, Z.K., Fraser-Harris, A., Edlmann, K., 2021. Modelling rock fracture induced by hydraulic pulses. Rock Mech. Rock Eng. 54 (8), 3977–3994. http://dx.doi.org/10.1007/s00603-021-02477-0.

Xiao, J.-Q., Ding, D.-X., Jiang, F.-L., Xu, G., 2010. Fatigue damage variable and evolution of rock subjected to cyclic loading. Int. J. Rock Mech. Min. 47 (3), 461–468. http://dx.doi.org/10.1016/j.ijrmms.2009.11.003.

Zang, A., Hofmann, H., Ji, Y., Zhuang, L., Lu, G., Bunger, A., 2025. How rock hydraulic fatigue methods from mining and petroleum industry assist in unlocking deep heat for a clean energy future. Renew. Sustain. Energy Rev. 217, 115683. http://dx.doi.org/10.1016/j.rser.2025.115683.

Zang, A., Zimmermann, G., Hofmann, H., Niemz, P., Kim, K.Y., Diaz, M., Zhuang, L., Yoon, J.S., 2021. Relaxation damage control via fatigue-hydraulic fracturing in granitic rock as inferred from laboratory-, mine-, and field-scale experiments. Sci. Rep. 11 (1), 6780. http://dx.doi.org/10.1038/s41598-021-86094-5.

Zhu, D., Jing, H., Yin, Q., Ding, S., Zhang, J., 2020. Mechanical characteristics of granite after heating and water-cooling cycles. Rock Mech. Rock Eng. 53, 2015–2025. http://dx.doi.org/10.1007/s00603-019-01991-6.

Zhuang, L., Kim, K.Y., Jung, S.G., Diaz, M., Min, K.B., Zang, A., Stephansson, O., Zimmermann, G., Yoon, J.S., Hofmann, H., 2019. Cyclic hydraulic fracturing of pocheon granite cores and its impact on breakdown pressure, acoustic emission amplitudes and injectivity. Int. J. Rock Mech. Min. 122, 104065. http://dx.doi.org/10.1016/j.ijrmms.2019.104065.

Zimmerman, R.W., Yeo, I.-W., 2000. Fluid flow in rock fractures: From the Navier–Stokes equations to the cubic law. In: Dynamics of Fluids in Fractured Rock. vol. 122, Wiley, pp. 213–224. http://dx.doi.org/10.1029/GM122p0213.